

Precursors_cci+

ESA Climate Change Initiative (CCI)



D2.1 Algorithm Theoretical Basis Document (ATBD)

Title	D2.1 Algorithm Theoretical Basis Document
Reference	Precursors_cci+_D2.1_ATBD_01_01
Issue	01
Revision	01
Status	Version 1
Date of issue	15/12/2023
Document type	Deliverable

This work has received funding from the European Space Agency under Contract No 4000138243 and is the result of the cooperation between the partners of the Precursors_cci+ consortium.





	FUNCTION	NAME	DATE
LEAD AUTHOR(S)	M. Van Roozendael	Folkert Boersma Sora Seo Pieter Valks Isabelle De Smedt Nicolas Theys Pascal Hedelt Thomas Danckaert Lieven Clarisse Martin Van Damme Cathy Clerbaux Maya George	15/12/2023
REVIEWED BY	Science Leaders	M. Van Roozendael Folkert Boersma	15/12/2023 15/12/2023
	ESA Project Officer	Simon Pinnock	.././....
DISTRIBUTED TO	ESA Precursors_cci+ Consortium		





DOCUMENT CHANGE RECORD

Issue	Revision	Date	Modified items	Observations
0	0	15/05/2023	Initial template	Creation of document
1	0	01/10/2023	First issue of the document (version 1.0), containing descriptions of the L2 algorithms for all products	
1	1	15/12/2023	Revision of document version 1 according to ESA RIDs of 18/10/2023	





Table of Contents

EXECUTIVE SUMMARY	9
1. PURPOSE AND SCOPE	10
1.1. Purpose	10
1.2. Scope	10
1.3. Applicable documents	10
1.4. Reference documents	10
1.5. List of acronyms	11
2. INSTRUMENTS	13
2.1. ERS-2/GOME	13
2.2. ENVISAT/SCIAMACHY	13
2.3. Sentinel-5P/TROPOMI	14
2.4. METOP/GOME-2	14
2.5. METOP/IASI	14
2.6. AURA/OMI	15
2.7. TERRA/MOPITT	15
3. LEVEL-2 ALGORITHMS	16
3.1. Tropospheric nitrogen dioxide (L2-NO ₂)	16
3.1.1. Overview	16
3.1.2. Algorithm description	16
3.1.3. NO ₂ slant column density retrieval	17
3.1.4. Separation of stratospheric and tropospheric NO ₂	20
3.1.5. Air mass factor and tropospheric NO ₂ column calculation	22
3.1.6. Information content and uncertainty estimate	26
3.2. Formaldehyde (L2-HCHO)	28
3.2.1. Flow diagram of the L2 retrieval algorithm	28
3.2.2. Slant Columns	29
3.2.3. Air Mass Factors	30
3.2.4. Background correction	30
3.2.5. Error estimate	32





3.3.	Sulfur dioxide (L2-SO ₂)	33
3.3.1.	Overview	33
3.3.2.	Algorithm description	34
3.3.3.	Information content and uncertainty estimate	38
3.4.	Glyoxal (L2-CHOCHO)	39
3.4.1.	Overview	39
3.4.2.	Algorithm description	40
3.4.3.	Information content and uncertainty estimate	45
3.5.	Carbon monoxide (L2-CO)	46
3.5.1.	Overview	46
3.5.2.	Algorithm description	46
3.5.3.	Uncertainty estimate	48
3.6.	Ammonia (L2-NH ₃)	49
3.6.1.	Retrieval overview	49
3.6.2.	HRI	51
3.6.3.	The neural network	55
3.6.4.	Averaging kernels	59
3.6.5.	Retrieval, uncertainty, and post-filtering	61
3.6.6.	Examples	63
3.6.7.	Advantages of the retrieval algorithm	65
3.6.8.	Comparison with an OEM retrieval	66
4.	LEVEL-3 ALGORITHMS	68
4.1.	Tropospheric nitrogen dioxide (L3-NO ₂)	68
4.1.1.	Overview	68
4.1.2.	Data gridding approach	68
4.1.3.	Inter-sensor bias analysis	68
4.1.4.	Data merging algorithm	68
4.1.5.	Uncertainty estimate	68
4.2.	Formaldehyde (L3-HCHO)	68
4.3.	Sulfur dioxide (L3-SO ₂)	68
4.4.	Glyoxal (L3-CHOCHO)	68
4.5.	Carbon monoxide (L3-CO)	68
4.6.	Ammonia (L3-NH ₃)	68
5.	REFERENCES	68

List of Figures

Figure 2-1: Overview of platforms and sensors used for the development and generation of CCI+ Precursors data records	13
Figure 3-1: General overview of the processing chain for the retrieval of the level-2 tropospheric NO ₂ columns.....	17
Figure 3-2: Timeseries of stratospheric and tropospheric NO ₂ over Europe derived with the data assimilation and STREAM approaches for GOME-2A. Tropospheric NO ₂ column values (indicated in red and green) have been divided by a factor of 4.....	21
Figure 3-3: Time series of the ratio of total tropospheric NO ₂ vertical column to clear-sky tropospheric NO ₂ vertical column retrieved using the OCRA/ROCINN and FRESCO v7 cloud products for GOME-2A over Europe.	24
Figure 3-4: Flow Diagram of the DOAS retrieval algorithm for HCHO.	28
Figure 3-5: Flow diagram of the SO ₂ column retrieval algorithm.	33
Figure 3-6: Glyoxal retrieval flowchart	39
Figure 3-7: Graphic representation of the processing steps. Satellite input data are in blue.	46
Figure 3-8: CO uncertainty time series for the globe, for day time and night time measurements, for both Metop-A and Metop-B.....	48
Figure 3-9: Conceptual flowchart of the ANNI retrieval method for NH ₃	50
Figure 3-10: Eigenvalue spectrum of the covariance matrix S_y used for the calculation of the HRI of NH ₃ . The eigenvalues are ordered from largest to smallest.	53
Figure 3-11: Monthly average HRI time series over 10 remote regions for the three IASI instruments separately. The top panel shows the uncorrected timeseries, and the other panels, from top to bottom, show the effects of the corrections that are applied consecutively.	55
Figure 3-12: Frequency distribution of NH ₃ total columns (left) and σ (right) values in the v3 and v4 training set.	57
Figure 3-13: Summary statistics on the training set: distribution of thermal contrast vs NH ₃ total columns (left), and spatial distribution vs thermal contrast (right).	57
Figure 3-14: Example of GEOS-Chem model (blue) and fitted (red) profiles (left) above a source area and (right) for transported NH ₃	57
Figure 3-15: Performance evaluation of the neural network, with added noise. The median value is shown in each grid box, which removes the effect of outliers to better reflect the real performance of the network.	59
Figure 3-16: Numerical demonstration of the linearity and additivity of the HRI as a function of a change in partial column. In the blue and green scenario, NH ₃ was varied at one fixed altitude. In the red scenario, partial columns in both layers were varied simultaneously. The black solid lines represent linearity, whereas the dash dotted line, being the sum of the green and blue curve, represents additivity.....	60
Figure 3-17: Example ERA5 climatology of the planetary boundary layer for April, morning (left) and evening (right).	62
Figure 3-18: Example NH ₃ retrievals from IASI-B on 24 April 2020 (AM, top; PM, bottom). Grey pixels are either cloudy or pixels that do not pass the post filter.	64



Figure 3-19: NH₃ seasonal average, derived from 0.5° by 0.5° monthly averages of the reanalysis product of ANNI v4. Data includes all measurements from IASI-A (October 2007 to December 2019), IASI-B (March 2013 to September 2022) and IASI-C (September 2019 to September 2022), with a cloud fraction below 10 %.65

Figure 3-20: Comparison between ANNI v4 NH₃ columns and retrievals based on optimal estimation for two scenes, one over Europe (top panels, 18 April 2013, Metop A morning overpass) and North America (bottom panels, 6 May 2021, Metop B morning overpass). The left panels depict the optimal estimation retrieved columns. The middle panels are scatter plots between the two retrievals, where each observation is colour coded according to thermal contrast (brightness temperature of the surface minus the temperature at half the boundary layer height). The right panels summarize the comparison by means of histograms of the differences.67





List of Tables

Table 3-1: Overview of NO₂ slant column density settings for morning sensors17

Table 3-2: Overview of NO₂ slant column density settings for afternoon sensors.....19

Table 3-3: Overview of stratospheric NO₂ estimation settings for morning sensors.21

Table 3-4: Selected settings for forward model parameters used in the calculation of tropospheric NO₂ AMFs in the ESA CCI ECV Precursor project for the morning sensors.25

Table 3-5: Selected settings for forward model parameters used in the calculation of tropospheric NO₂ AMFs in the ESA CCI ECV Precursor project for the afternoon sensors.25

Table 3-6: Estimation of the uncertainty contributions to the overall, per-pixel tropospheric NO₂ column uncertainty over polluted regions.27

Table 3-7: Settings used for DOAS spectral fitting for the different satellite instruments.29

Table 3-8: Input used for AMF calculation for the different satellite instruments.30

Table 3-9: Background correction settings for the different satellite instruments. To be updated.....31

Table 3-10: Settings used for COBRA spectral fitting for the different satellite instruments used (preliminary).....36

Table 3-11: Criteria for selecting alternative fitting windows.36

Table 3-12: Input parameters used for AMF calculation and the for the different satellite instruments used (preliminary).....37

Table 3-13: Estimation of the error sources of the SO₂ COBRA retrieval (preliminary) for typical polluted conditions, at low/high SZA (latitudes). Blue and red fields indicate random (precision) and systematic (trueness) errors. Total errors are computed assuming all contributions are mutually uncorrelated.38

Table 3-14: Selected pacific background region for daily reference radiance per instrument.40

Table 3-15: Absorption cross sections.....40

Table 3-16: Radiative transfer input data per sensor.....41

Table 3-17: Glyoxal tropospheric vertical column density retrieval uncertainty components 45

Table 3-18: Summary of the origin of the ANNI input parameters for NH₃.62





Executive Summary

The Algorithm Theoretical Basis Document (ATBD, deliverable D2.1 in Precursors_cci+) describes the algorithms used for the generation of the NO₂, HCHO, SO₂, glyoxal (CHOCHO), CO and NH₃ data products. The document covers level-2 and level-3 algorithms and includes descriptions of the sensors used, retrieval methods applied, ancillary data sets as well as a synthetic description of the uncertainty budget. A detailed analysis of the uncertainty budget is provided separately in the End-to-End ECV Uncertainty Budget document (E3UB) (D2.2).



1. Purpose and scope

1.1. Purpose

This document describes the retrieval algorithms used in the Precursors_cci+ project. It addresses six important precursors of ozone and aerosol ECVs, namely: tropospheric NO₂, HCHO, CO, SO₂, NH₃ and glyoxal.

1.2. Scope

The scope of the ATBD is to fully describe each retrieval algorithm used to derive the ECV products from input satellite data. This includes descriptions of input satellite data and ancillary data, retrieval methods and procedures including pre- or post-processing steps, and a general overview of the processing chain applied for each trace gas product. The ATBD addresses both level-2 and level-3 retrieval algorithms.

1.3. Applicable documents

- [AD-1] Data Standards Requirements for CCI Data Producers. Latest version at time of writing is v1.2: ref. CCI-PRGM-EOPS-TN-13-0009, 9 March 2015, available online at: https://climate.esa.int/media/documents/CCI_DataStandards_v2-3.pdf
- [AD-2] CCI Data Policy v1.1. Available online at: https://climate.esa.int/sites/default/files/CCI_Data_Policy_v1.1.pdf

1.4. Reference documents

- [RD-1] GCOS Climate Monitoring Principles, November 1999. Available online at: <https://gcos.wmo.int/en/essential-climate-variables/about/gcos-monitoring-principles>
- [RD-2] Guideline for the Generation of Satellite-based Datasets and Products meeting GCOS Requirements, GCOS Secretariat, GCOS-128, March 2009 (WMO/TD No. 1488). Available online at: https://library.wmo.int/index.php?lvl=notice_display&id=12884#.Yw4rL7RByUk
- [RD-3] Quality assurance framework for earth observation (QA4EO): <http://qa4eo.org>
- [RD-4] The Global Observing System for Climate: Implementation Needs, GCOS-200, October 2016. Available online at: <https://gcos.wmo.int/en/gcos-implementation-plan>
- [RD-5] Status of the Global Observing System for Climate, GCOS-195, October 2015. Available online at: https://library.wmo.int/index.php?lvl=notice_display&id=18962#.Yw4r8LRByUk



- [RD-6] Hollmann, R., et al., The ESA climate change initiative: Satellite data records for essential climate variables. American Meteorological Society. Bulletin, Vol. 94, No. 10, 2013, p. 1541-1552.
- [RD-7] Joint Committee for Guides in Metrology, 2008, Evaluation of measurement data — Guide to the expression of uncertainty in measurement (GUM), JCGM 100: 2008. Available online at: <https://www.iso.org/sites/JCGM/GUM-JCGM100.htm>
- [RD-8] Merchant, C., et al., 2017, Uncertainty information in climate data records from Earth observation, Earth Syst. Sci. Data Discuss., vol. 9, p511-527

1.5. List of acronyms

AC-SAF	Satellite Application Facility on Atmospheric Composition Monitoring
ADP	Algorithm Development Plan
AK	Averaging Kernel
AMF	Air-mass factor
ATBD	Algorithm Theoretical Basis Document
BIRA-IASB	Royal Belgian Institute for Space Aeronomy
BIRA-IR	BIRA-IASB Infrared Team
BIRA-SYN	BIRA-IASB Synergy Team
BIRA-UVVIS	BIRA-IASB UV-Vis Team
BIRA-MOD	BIRA-IASB Tropospheric Modeling Team
CAMS	Copernicus Atmospheric Monitoring Service
C3S	Copernicus Climate Change Monitoring Service
CCI	ESA Climate Change Initiative
CCI+	Climate Change Initiative Extension (CCI+), is an extension of the CCI over the period 2017-2024.
CEOS	Committee on Earth Observation Satellites
CMUG	Climate Modeling User Group
CO	Carbon monoxide
COBRA	COvariance-Based Retrieval Algorithm
CRDP	Climate Research Data Package
CRG	Climate Research Group
DLER	Directional Lambertian Equivalent Reflectance
DLR	German Aerospace Centre
DOAS	Differential Optical Absorption Spectroscopy
ECMWF	European Centre for Medium-range Weather Forecast
ECV	Essential Climate Variable
ENVISAT	Environmental Satellite (ESA)
EO	Earth Observation
ESA	European Space Agency
EU	European Union





EUMETSAT	European Organisation for the Exploitation of Meteorological Satellites
FCDR	Fundamental Climate Data Record
FRESCO	Fast Retrieval Scheme for Clouds from the Oxygen A band
FRM	Fiducial Reference Measurement
GCOS	Global Climate Observation System
GOME	Global Ozone Monitoring Instrument (aboard ERS-2)
GOME-2	Global Ozone Monitoring Instrument – 2 (aboard MetOp-A, -B and -C)
IASI	Infrared Atmospheric Sounding Interferometer
HRI	Hyperspectral Range Index
KNMI	Royal Netherlands Meteorological Institute
LEO	Low Earth Orbit
LER	Lambertian Equivalent Reflectance
LUT	Look-up table
Metop	Meteorological Operational Platform (EUMETSAT)
MOPITT	Measurement of Pollution in the Troposphere
NASA	National Aeronautics and Space Administration
NDACC	Network for the Detection of Atmospheric Composition Change
NH ₃	Ammonia
NN	Neural Network
NO ₂	Nitrogen dioxide
NRT	Near-Real Time
OCRA	Optical Cloud Recognition Algorithm)
OMI	Ozone Monitoring Instrument (aboard EOS-Aura)
PCA	Principal Component Analysis
QA4ECV	Quality Assurance for Essential Climate Variables
QA4EO	Quality Assurance framework four Earth Observation
R&D	Research and Development
ROCINN	Retrieval of Cloud Information using Neural Networks
SAF	Satellite Application Facility
SCIAMACHY	Scanning Imaging Absorption Spectrometer for Atmospheric
S5P	Sentinel-5 Precursor
SoW	Statement of Work
STREAM	STRatospheric Estimation Algorithm from Mainz
SZA	Solar Zenith Angle
TEMIS	Tropospheric Emission Monitoring Internet Service
TIR	Thermal Infrared spectral range
TROPOMI	Tropospheric Monitoring Instrument (aboard Sentinel-5 Precursor)
TOA	Top-of-atmosphere
TOAR-II	Tropospheric Ozone Assessment Report Phase-II
ULB	Université Libre de Bruxelles
IUP-UB	Institute of Environmental Physics, University of Bremen
UPAS	Universal Processor for UV/Vis Atmospheric Sensors
UV-Vis	Ultraviolet and visible spectral range



WP

Work Package





the stratosphere (Bovensmann et al., 1999). The solar radiation transmitted, backscattered and reflected from the atmosphere is recorded at medium resolution (0.2 nm to 1.5 nm) over the range 240 nm to 1700 nm, and in selected regions between 2.0 μm and 2.4 μm . SCIAMACHY is particular since it has three different viewing geometries: nadir, limb, and sun/moon occultation, which yield total column values as well as distribution profiles in the stratosphere and upper troposphere. In this project both nadir and limb measurements are used in Channels 1, 2 and 3. In nadir view, used for ozone total column and vertical profile retrievals, the ground pixel size for channels 2-3 is 30x60 km^2 , i.e. a resolution intermediate between GOME and OMI. The swath width of SCIAMACHY at nadir is similar to GOME (960 km), however due to the alternate nadir and limb mode operation, global coverage is only obtained in approximately 6 days. In limb view, ozone number density profiles are derived in the stratosphere by exploiting the Hartley and Chappuis spectral absorption bands in channels 1 and 3. SCIAMACHY data are available from July 2002 till April 2012 when communication with ENVISAT was lost.

2.3. Sentinel-5P/TROPOMI

The TROPOMI instrument is a space-borne, nadir-viewing, imaging spectrometer covering wavelength bands between the ultraviolet and the shortwave infrared. It is the single payload of Sentinel-5 Precursor, the first Copernicus mission dedicated to the monitoring of atmospheric composition. Launched on 13 October 2017 for a mission of minimum seven years, it operates in a push-broom configuration (non-scanning), with a swath width of ~ 2600 km on the Earth's surface. The TROPOMI instrument is similar in concept to OMI, but it offers a much-improved spatial resolution of about 5.5x3.5 km^2 at nadir, with similar or better radiometric performance than OMI. Covering the ultraviolet (UV), visible (VIS), near (NIR) and short-wavelength infrared (SWIR), it provides daily global measurements of a number of gases in the atmosphere, including ozone, methane (CH_4), HCHO, NO_2 , SO_2 , aerosol and carbon monoxide (CO).

2.4. METOP/GOME-2

The first GOME-2 instrument was launched on-board the EUMETSAT satellite Metop-A in October 2006 (Munro et al., 2016). Built on a design almost identical to GOME, it covers the same spectral range as its predecessor but with an improved spatial resolution. The nominal ground-pixel size is 80 x 40 km^2 with a global coverage in almost one day (swath of 1920 km). GOME-2 continues the measurement series started with GOME, and in this project it is therefore used to retrieve total columns and vertical distributions of ozone. Data are available since January 2007 on an operational basis. A second GOME-2 instrument was launched in 2012 on the Metop-B platform, and a third one was launched in November 2018 on Metop-C.

2.5. METOP/IASI

The Infrared Atmospheric Sounding Interferometer (IASI) is a nadir looking Fourier Transform Spectrometer associated with an imaging instrument launched on the Metop series of European meteorological EUMETSAT's polar-orbit satellites. The mission is dedicated to high-



resolution atmospheric sounding of trace gases like ozone, methane or carbon monoxide on a global scale and to operational meteorological soundings with a high accuracy requirement (1 K for tropospheric temperature and 10% for humidity with a vertical resolution of 1 km). Three IASI instruments have been successively launched in October 2006, in September 2012 and in November 2018 on Metop-A, -B and -C respectively. The Metop satellites are sun-synchronous with a 98.7° inclination to the equator, and a global coverage twice daily at about 09:30 and 21:30 local time. Each of the three launched Metop platforms makes a little more than 14 orbits a day. IASI is a cross-track scanner covering the infrared spectral domain from 645 to 2,760 cm^{-1} (3.62–15.5 μm) with a total of 30 ground fields of regard (FOR) per scan. The spectrum is measured in three wavelength bands (8.26–15.5, 5.0–8.26, and 3.62–5.0 μm), with a separate detector allowing the continuous spectral coverage with no gaps, and each FOR measures a 2x2 array of footprints characterized by a 12-km diameter at nadir. The apodized spectral resolution is 0.5 cm^{-1} and each spectrum is sampled every 0.25 cm^{-1} providing a total of 8461 radiance channels.

2.6. AURA/OMI

The Ozone Monitoring Instrument (OMI) is a nadir viewing imaging spectrograph that measures the solar radiation backscattered by the Earth's atmosphere and surface over the entire wavelength range from 270 to 500 nm with a spectral resolution of about 0.5 nm. OMI was launched on-board the NASA satellite AURA in July 2004. In comparison to the GOME and SCIAMACHY sensors, OMI is characterized by a larger swath width of 2600 km, which enables measurements with a daily global coverage at all latitudes. The nominal OMI pixel size of 13 x 24 km^2 at nadir is also significantly smaller. The small pixel size enables OMI to look in between the clouds, which is important for retrieving tropospheric information. The light entering the telescope is also depolarised using a scrambler, which avoids polarization-related artefacts. OMI data are available since 2004 and the instrument is still operational, however in 2007 OMI started to experience the so-called row anomaly which reduces the amount of useful measurements, despite correction algorithms being implemented in the level-1 processing chain.

2.7. TERRA/MOPITT

MOPITT (Measurement of Pollution in the Troposphere) is one of the earliest satellite sensors to use gas correlation spectroscopy. It is a nadir sounding (vertically downward pointing) instrument that measures upwelling infrared radiation at 4.7 μm and 2.2-2.4 μm . It was launched on the NASA Terra satellite in December 1999. The Terra satellite is in a 705-km, sun-synchronous orbit with a 10:30 a.m. equator crossing time.

The MOPITT sensor measures emitted and reflected radiance from the Earth in three spectral bands. As this light enters the sensor, it passes along two different paths through onboard containers of carbon monoxide. The different paths absorb different amounts of energy, leading to small differences in the resulting signals that correlate with the presence of these gases in the atmosphere. MOPITT's spatial resolution is 22 km at nadir with a swath of 640 km



wide. It can measure the concentrations of carbon monoxide in 5-km layers down a vertical column of atmosphere, to help scientists track the gas back to its sources.



3. Level-2 algorithms

3.1. Tropospheric nitrogen dioxide (L2-NO₂)

3.1.1. Overview

The level-2 algorithms used to generate a tropospheric nitrogen dioxide product from the GOME, SCIAMACHY, GOME-2, OMI and TROPOMI sensors are based on the DOAS-approach and follow the same retrieval principles. The L2-NO₂ data products have the tropospheric NO₂ column density as their main retrieval outcome, but also provide the stratospheric vertical column and total vertical column density. The algorithms provide geophysical data for every ground pixel observed by the 5 sensors. In addition to the vertical columns, the L2_NO₂ dataset will contain retrieval uncertainty estimates for every pixel, and information on intermediate retrieval steps, such as the spectral fitting result and diagnostics, and information on factors that have influenced the retrieval such as clouds, surface reflectance, and the vertical distribution of NO₂.

3.1.2. Algorithm description

The NO₂ retrieval procedure consists of a procedure with three steps, and is performed for each level-1 spectrum:

- (1) Retrieval of the total NO₂ slant column density (N_s) from the level-1 radiance and irradiance spectra measured by the sensor with the Differential Optical Absorption Spectroscopy (DOAS) method,
- (2) Separation of the N_s into a stratospheric (N_s^{strat}) and tropospheric part ($N_s^{trop} = N_s - N_s^{strat}$) based on information from a system incorporating slant columns and modelled or climatological information on tropospheric contributions,
- (3) Conversion of the tropospheric slant column density into a vertical column density (N_v^{trop}) via a tropospheric air mass factor (M^{trop}).

The central retrieval equation can thus be written as:

$$N_v^{trop} = \frac{N_s - N_s^{strat}}{M^{trop}} \quad \text{Eq. 3-1}$$

In Eq. 3-1 the factor M^{trop} quantifies how the tropospheric slant column has been influenced by scattering, absorption, and reflection in the troposphere or by the Earth's surface. M^{trop} depends on the satellite viewing geometry, the presence of clouds or aerosols, surface properties, and the vertical distribution of NO₂ in the troposphere. The retrieval procedure therefore requires accurate, pixel-specific information on these geophysical parameters, and the NO₂ level-2 algorithms obtain this from the satellite measurements themselves, or from well-tested ancillary datasets.



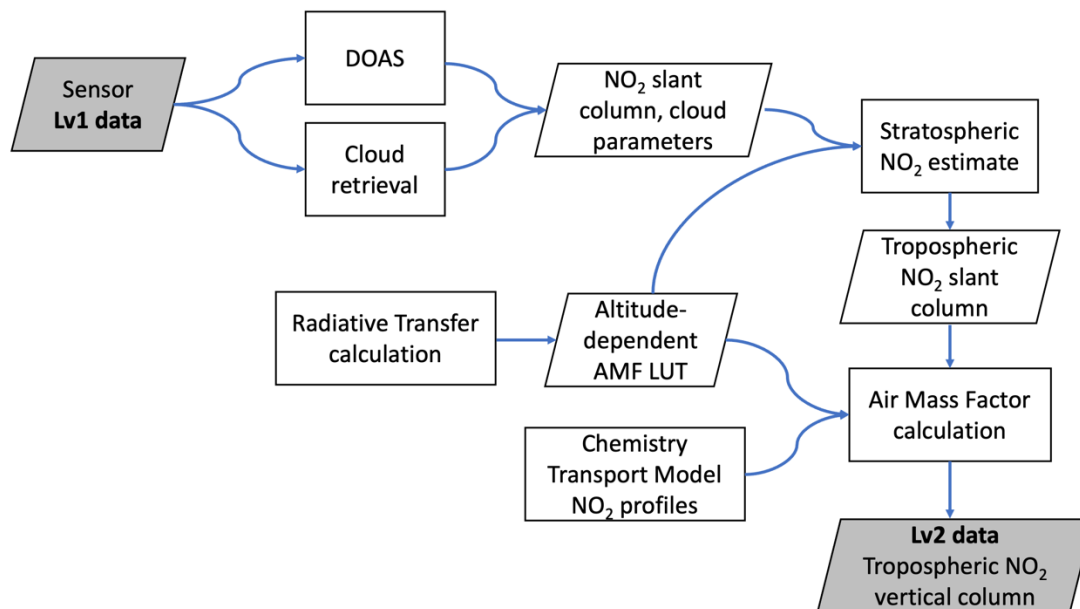


Figure 3-1: General overview of the processing chain for the retrieval of the level-2 tropospheric NO₂ columns.

For all 5 sensors, the retrieval procedure for NO₂ is identical in terms of retrieval steps. But because of instrumental differences in terms of overpass time, spectral range, calibration issues and limitations in terms of processing capacity, different approaches are required for different instruments in some cases. In what follows, we describe what actions have been taken to ensure as much as possible consistency between level-2 NO₂ products.

3.1.3. NO₂ slant column density retrieval

The approach to determine NO₂ slant column densities from level-1 data is DOAS. The below tables summarize the settings selected for NO₂ slant column density retrieval for each of the five morning sensors (Table 3-1) and the two afternoon sensors (Table 3-2).

Table 3-1: Overview of NO₂ slant column density settings for morning sensors

	GOME	SCIAMACHY	GOME-2A	GOME-2B	GOME-2C
Level-1 version	v5.1	v8	v6.3	v6.3	v6.3
Fitting window	425-465 nm	425-465 nm	425-497 nm	425-497 nm	430-465 nm ¹
Fitting method	Optical density	Optical density	Optical density	Optical density	Optical density

¹ Systematic offsets between GOME-2C and GOME-2A/B slant columns because of level-1 issues in GOME-2C. To ensure consistency in NO₂ slant columns between the three instruments, a different spectral fitting window was selected for GOME-2C.



Solar reference	Daily Pacific radiance spectrum ²	Daily solar reference using ASM diffusor	SAO solar reference in vacuum ³	SAO solar reference in vacuum	SAO solar reference in vacuum
Polynomial	4 th order	4 th order	5 th order	5 th order	4 th order
Fitting parameters	NO ₂ , O ₃ , O ₂ -O ₂ , H ₂ O, Ring, liquid water	NO ₂ , O ₃ , O ₂ -O ₂ , H ₂ O, Ring, liquid water	NO ₂ , O ₃ , O ₂ -O ₂ , H ₂ O, Ring, liquid water	NO ₂ , O ₃ , O ₂ -O ₂ , H ₂ O, Ring, liquid water	NO ₂ , O ₃ , O ₂ -O ₂ , H ₂ O, Ring, liquid water
Undersampling correction	Yes	No	No	No	No
Eta correction	Yes	No	Yes ⁴	Yes	Yes
Reference	Boersma et al. (2018)	Boersma et al. (2018)	Liu et al. (2019)	Liu et al. (2019)	Valks et al. (2019)

Most settings are highly consistent between the morning sensors. Previous tests indicated excellent consistency between GOME and SCIAMACHY NO₂ slant columns despite different usage of solar reference (QA4ECV D4.5 – Figure 20). Georgoulas et al. (2019) showed that the (QA4ECV) data products from GOME, SCIAMACHY and GOME-2A are fit-for-purpose of monitoring long-term trends in tropospheric NO₂ columns, a further indication of good consistency of the NO₂ slant columns.

Tests in the Round Robin phase in this project showed very good consistency between NO₂ slant columns from GOME-2A and GOME-2B derived with the 425-497 nm window. The selection of this window however is a notable change relative to the 405-465 nm window used for GOME-2A in the QA4ECV-project. Round Robin tests indicated that the NO₂ slant columns obtained from the 405-465 nm spectral window show a good overall consistency with those from the 425-497 nm window (used in the AC-SAF prototype). However, after June 2015, the GOME-2A NO₂ slant columns from the 405-465 nm window show substantial sensitivity to the updated v6.1 (and later versions) GOME-2A level-1b data, diagnosed as stronger seasonality and ‘jumps’ in NO₂ slant column over background areas. Small uncertainties and high robustness in GOME-2A NO₂ slant columns are obtained with the 425-497 nm window and with the v6.3 level-1 data also after June 2015. This fitting window, in conjunction with the v6.3 level 1b data also significantly reduces the inter-instrument bias between GOME-2A and GOME-2B, which is why they are the recommended setting for GOME-2 retrievals in the ESA CCI+ ECV Precursor project.

For GOME-2 on MetOp-C, an alternative fitting window 430 - 465 nm is used. This adjustment was made due to a significant (~40%) positive offset observed between NO₂ slant columns from GOME-2C and GOME-2A/B when applying an identical fitting window (EUMETSAT, 2019).

² The Pacific Ocean reference sector is the region enclosed by 10° S – 10° N, 160° E – 100° W, +1.476 10¹⁵ molec.cm⁻² in reference spectrum

³ sao_solref_vac

⁴ Eta and Zeta from GOME-2 calibration key data



This offset is related to systematic structures in the DOAS fitting residual for GOME-2C at wavelengths < 430 nm. By shifting the start wavelength for GOME-2C to 430 nm and the end wavelength to 465 nm, the inter-instrument bias in NO₂ slant columns between GOME-2C and GOME-2A/B is effectively reduced, while maintaining a high signal-to-noise.

The spectral fitting settings selected for the afternoon sensors OMI and TROPOMI are indicated in Table 3-2. For OMI, most settings are consistent with those used within the QA4ECV project. However, since that project ended, a new OMI level-1 data set has become available (Kleipool et al., 2022) in line with developments for TROPOMI. The new collection-4 level-1 data comprise a clear improvement relative to the previous OMI level-1 data and will be used as starting point for the spectral fitting from OMI. A second deviation with respect to the QA4ECV OMI NO₂ spectral fitting is that the set of fitting parameters no longer includes the intensity offset correction. Including such a term in the spectral fitting has been shown to impact the NO₂ slant columns up to 1×10^{15} molec.cm⁻² (QA4ECV D4.2) over clean ocean scenes, where the term accounts for spectral structures associated with vibrational Raman scattering in water and results in smaller uncertainties and somewhat lower NO₂ slant columns (Oldeman, 2018). Leaving out the intensity offset term in the spectral fitting however has the advantage of making the OMI DOAS fit consistent with the TROPOMI DOAS fit (van Geffen et al., 2022).

Table 3-2: Overview of NO₂ slant column density settings for afternoon sensors.

	OMI	TROPOMI
Level-1 version	Coll004	v2.0
Fitting window	405-465 nm	405-465 nm
Fitting method	Optical density	Optical density
Solar reference	Annual mean solar reference	
Polynomial	4 th order	4 th order
Fitting parameters	NO ₂ , O ₃ , O ₂ -O ₂ , H ₂ O, Ring, liquid water	NO ₂ , O ₃ , O ₂ -O ₂ , H ₂ O, Ring, liquid water
Undersampling correction	No	No
Eta correction	No	No
Reference	Boersma et al. (2018)	van Geffen et al. (2021) van Geffen et al. (2022)

The temperature for the absorption cross-section spectra of the fitting parameters is fixed. The spectral shape of these cross-section spectra usually does not change with temperature, but for NO₂, the amplitude decreases with increasing atmospheric temperature (Boersma et al., 2004). The final NO₂ slant column densities therefore need to be corrected for deviations of the effective atmospheric NO₂ temperature from T = 220 K, at which the NO₂ cross section was measured as used in most spectral fitting retrievals. This correction requires knowledge of vertical NO₂, temperature, and sensitivity profiles and is therefore done at step 3 – the air mass factor calculation- of the retrieval (Figure 3-1).



OMI and TROPOMI NO₂ SCDs showed across-track biases, or stripes, due to small detector viewing angle dependent differences in calibration parameters. A destriping approach, integrated in the retrieval algorithm, is applied after the retrieval of the SCDs. The destriping correction is determined from orbits over the Pacific Ocean (150 – 180 W over 30 belt in the Tropics). Subsequently, the NO₂ SCDs are corrected by subtracting the stripe amplitude correction. Further details can be found in Boersma et al. (2011), Boersma et al. (2018), and van Geffen et al. (2022).

3.1.4. Separation of stratospheric and tropospheric NO₂

The next major algorithm step in the level-2 algorithm is the estimation of the stratospheric NO₂ column density. The Round Robin outcome, recommendations from the QA4ECV project, and recent validation studies (Verhoelst et al. (2021); Wang et al. (2020); Compernelle et al. (2020); Hendrick et al. (2012)) pointed out that there are only small differences between forecast stratospheric NO₂ based on **data assimilation** of NO₂ slant columns in TM5-MP (Dirksen et al., 2011) and daily smoothed stratospheric NO₂ estimated with the **STREAM** approach (Beirle et al., 2016). Based on this body of evidence we consider both data assimilation and STREAM viable approaches to separate the stratospheric from the tropospheric NO₂ signal for the retrievals in this project. Practical considerations dictate that L2-retrievals performed at KNMI use data assimilation and those performed at DLR use STREAM. Table 3.3 below provides an overview of the algorithm settings and inputs for the morning sensors. For the afternoon sensors, both retrieval algorithms are operated at KNMI, data assimilation will be used as in the QA4ECV and S5P projects.

The methods to estimate stratospheric NO₂ resemble one another in that they use a similar weighting scheme, which effectively screens slant columns retrieved over polluted regions and regions with substantial tropospheric NO₂ background. There are some differences between the two approaches, which are worth emphasizing:

- Data assimilation provides a stratospheric NO₂ field which is model-predicted, but strongly rooted in an observation-driven system.
- STREAM provides a smoothed, spatially interpolated stratospheric NO₂ field, which is based on daily observations, and on assumptions that spatial variability in stratospheric NO₂ is generally smooth.

Figure 3-2 illustrates the good consistency between the data assimilation and STREAM methods in estimating the stratospheric NO₂ amounts over Europe from GOME-2A. After June 2015, the discrepancies between data assimilation and STREAM increase somewhat, especially in summer, but this mainly reflects systematic differences in the input NO₂ slant column datasets used in the two retrievals tested in the Round Robin.

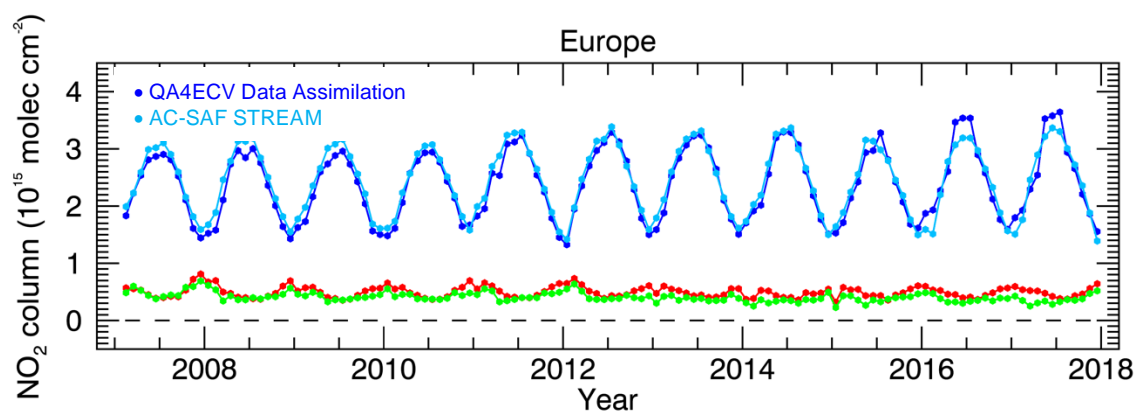


Figure 3-2: Timeseries of stratospheric and tropospheric NO₂ over Europe derived with the data assimilation and STREAM approaches for GOME-2A. Tropospheric NO₂ column values (indicated in red and green) have been divided by a factor of 4.

Data assimilation in TM5-MP

The L2 retrievals at KNMI use data assimilation of NO₂ slant columns in the TM5-MP chemistry transport model (Williams et al., 2017). This system incorporates observed information on NO₂ slant columns, clouds, and estimates of surface reflectivity to update the TM5-MP simulation of the 3-D global NO₂ distribution in such a way that the model simulation of stratospheric NO₂ comes in close agreement with the satellite observations, especially over regions with background levels of tropospheric NO₂ that are dominated by stratospheric NO₂. The assimilation scheme is based on the Kalman-filter technique, in which the TM5-MP model state is adjusted towards the observations, providing a new analysis of the model state for every orbit. For a detailed description of the Kalman filtering, see Eq. (1) and Figure 1 in Dirksen et al. (2011), and recent developments are described in van Geffen et al. (2022). Because satellite observations over pristine regions with low amounts of tropospheric NO₂ receive more weight, the filtering approach leads to relatively strong forcing of the simulated stratospheric NO₂ concentrations towards the satellite observations and will result only in marginal adjustment of the simulated tropospheric NO₂ field over polluted regions.

STREAM

The L2 retrievals at DLR use the STRatospheric Estimation Algorithm from Mainz (STREAM) method, developed by Beirle et al. (2016). This is an improved modified reference sector method. A reference sector method has shortcomings in larger uncertainties over polluted areas since this uses measurements over clean regions with assumptions of longitudinally invariable stratospheric NO₂ columns and of negligible tropospheric NO₂ abundance (e.g. Boersma et al. (2004)). Instead of binary masks based on arbitrary thresholds, STREAM applies a weighted convolution scheme where cloudy observations are given a high weight and polluted observations are given low weight. The STREAM method has been adapted to GOME-2 measurements by calculating weighting factors for each satellite pixel to define the contribution of initial total columns to the stratospheric estimation based on a tropospheric NO₂ climatology and the GOME-2 cloud product (Liu et al., 2019).

Table 3-3: Overview of stratospheric NO₂ estimation settings for morning sensors.

	GOME	SCIAMACHY	GOME-2A	GOME-2B	GOME-2C
Method	Data assimilation	Data assimilation	STREAM	STREAM	STREAM
Use of CTM	Yes	Yes	No	No	No
Spatial convolution	No	No	Yes	Yes	Yes
Accounts for diurnal cycle in stratospheric NO₂	Yes	Yes	No	No	No
Correction for residual tropospheric contribution to NO₂ SCD	Yes	Yes	No	No	No

3.1.5. Air mass factor and tropospheric NO₂ column calculation

The tropospheric NO₂ algorithms use as default pre-calculated air mass factor look-up tables to convert slant columns into meaningful vertical columns (Lorente et al., 2017). The AMF (M) is the ratio of the slant column density of the absorbing gas along the (slant) optical path from the Sun to the satellite and the vertical column density above the surface area (pixel) the satellite is viewing. The tropospheric air mass factor follows from the ratio of the slant column density and vertical column density modelled with a radiative transfer model:

$$M_{tr} = \frac{N_{s,tr}}{N_{v,tr}} \quad \text{Eq. 3-2}$$

The tropospheric air mass factor depends on the vertical profile of the trace gas and can be written as (Palmer et al. (2021); Eskes and Boersma (2003)):

$$M_{tr} = \frac{\sum_l m_l n_l c_l}{\sum_l n_l} \quad \text{Eq. 3-3}$$

With m_l the altitude-dependent AMFs or bob-AMFs describing the vertically resolved sensitivity to NO₂ in layer l , n_l the vertical column density in layer l , and c_l the temperature correction term discussed in section 3.1.3. The summation in Eq. 3-3 takes place over all vertical layers in the troposphere. The altitude-dependent AMFs depend on retrieval parameters, including the satellite viewing geometry, as well as the forward model parameters surface albedo (a_s), surface pressure (p_s), (effective) cloud fraction (f_{cl}), and



(effective) cloud pressure (p_{cl}), so M_{tr} can be written as a function of the set of forward model parameters ($a_s, p_s, f_{cl}, p_{cl}, \mathbf{n}$) with \mathbf{n} a vector indicating the a priori tropospheric vertical profile.

Altitude-dependent AMFs

The altitude-dependent AMFs, or vertical sensitivities, have been calculated with a radiative transfer model by including a small, optically thin amount of NO₂ to the model atmosphere layer l for an atmosphere that is otherwise devoid of NO₂. The value for m_l is then given by ratioing the excess NO₂ slant column to the vertical column added to that layer ($m_l = \delta N_{s,l} / \delta N_{v,l}$). The radiative transfer model atmosphere does not include aerosols and describes the Earth's surface as a Lambertian reflector.

The altitude-dependent AMFs for the GOME, SCIAMACHY, OMI, and TROPOMI retrievals have been calculated with the Doubling-Adding KNMI (DAK) radiative transfer model (De Haan et al. (1987); Stammes et al. (2001)) version 3.2 at 437.5 nm, which includes a pseudo-sphericity correction, and a posterior correction against the full-sphericity model McArtim to better account for extreme viewing geometries (Boersma et al., 2018). Altitude-dependent AMFs for the GOME-2 retrievals have been generated by the VLIDORT radiative transfer model at 461 nm. The altitude-dependent AMFs are stored as a function of pre-define surface albedo, terrain height, solar zenith angle, viewing zenith angle, relative azimuth angles, and layer-height. Then, with the best available quantitative information on the values of these parameters, altitude-dependent AMFs for the clear-sky situation and for the cloudy-sky portion of a pixel (if present) are obtained by multi-dimensional interpolation in the look-up table. Quantities and reference points in the AMF look-up table calculated with DAK can be found in Table 4 in van Geffen et al. (2022).

Correction for cloud cover

It is important to account for the effect of clouds when calculating tropospheric AMFs in the presence of clouds. We calculate AMFs in (partly) cloudy situations via the independent pixel approximation (IPA, Martin et al. (2002)):

$$M_{tr} = (1 - w)M_{clear} + wM_{cl} \quad \text{Eq. 3-4}$$

with w the the cloud radiance fraction (the portion of radiance coming from the cloudy part of the pixel):

$$w = \frac{f_{cl}I_{cl}}{R} = \frac{f_{cl}I_{cl}}{f_{cl}I_{cl} + (1 - f_{cl})I_{clear}} \quad \text{Eq. 3-5}$$

where I_{cl} is the radiance coming from the cloudy part of the pixel, I_{clear} the radiance from the clear part of the pixel, and the R total scene radiance. M_{clear} represents the clear-sky



(tropospheric) AMF, and M_{cl} the cloudy-sky (tropospheric) AMF. The main motivation for using Eq. 3-4 to calculate the tropospheric AMF is that very few pixels are completely cloud-free, especially for the historical sensors. The relevant physical effects, reduced sensitivity to NO_2 below the cloud level ('screening') and enhanced sensitivity to NO_2 above the cloud ('albedo effect') are explicitly accounted for in this independent pixel approximation. The cloud radiance can be determined from the radiance in the NO_2 fit window, or via the analytical approach of Vermote and Tanre (1992), using the effective cloud fraction f_{cl} from the cloud retrieval process for the sensor of interest.

Table 3.4 summarizes the selection of information sources for ancillary data (or forward model parameters) on the atmospheric state needed for each pixel to calculate the tropospheric AMF M_{tr} via the recipe of Eq. 3-2 - Eq. 3-5 above.

To allow for future accounting for the viewing angle dependency of surface albedo, the GOME-2 DLER dataset (Tilstra et al., 2021) was adopted. This dataset is derived by dividing the GOME-2 orbit swath into five segments and retrieving the traditional surface LER for each segment based on the data from the respective part of orbit swath. The GOME-2 DLER dataset improves the underestimation of the surface albedo on the western side of the GOME-2 orbit and increases AMFs by up to 15 % in polluted regions compared to the previous GOME-2 surface LER climatology (Liu et al., 2020).

The NO_2 retrieval is affected by the presence of clouds with high clouds shielding underlying parts of the atmosphere and low clouds contributing enhancements in NO_2 absorption due to multiple scattering and albedo effects. To account for cloud effects in GOME-2 NO_2 retrieval, cloud corrections are applied using the OCRA/ROCINN cloud parameters (Lutz et al, 2016; Loyola et al, 2018). During the Round Robin exercise, we compared the impact of cloud correction on the GOME-2 AMF using OCRA/ROCINN and FRESCO v7 for the GOME-2A mission period. Generally, cloud corrections from both OCRA/ROCINN and FRESCO are similar. However, cloud corrections using cloud parameters from OCRA/ROCINN result in up to 10% higher tropospheric NO_2 columns in polluted regions (Europe), reflecting higher OCRA/ROCINN cloud heights leading to a stronger 'screening effect' in the AMF calculation, as shown in Figure 3-3. For clean areas, the difference in the impact on the cloud corrections between the two cloud products is relatively small, ~5 %.

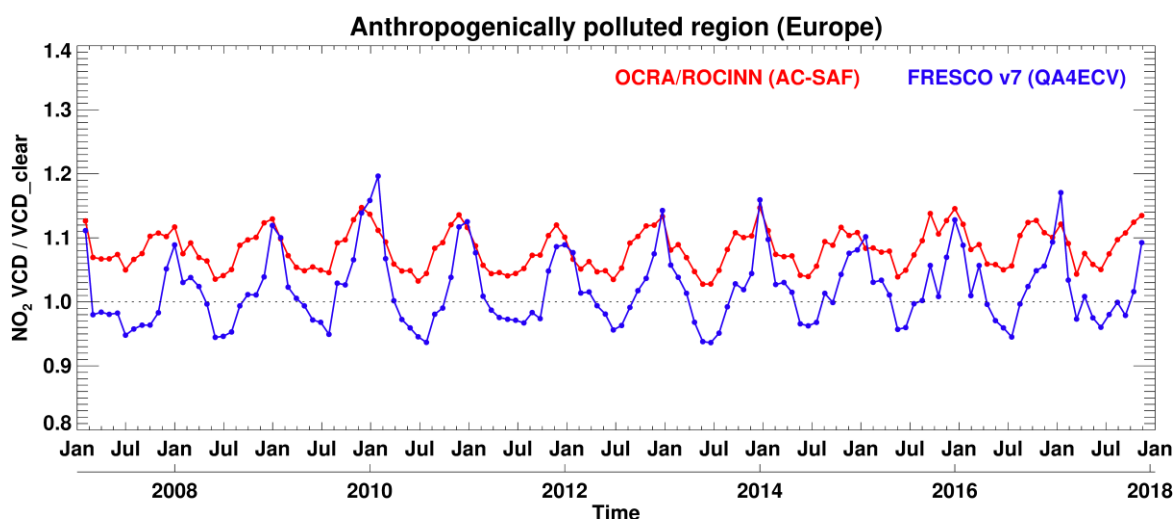


Figure 3-3: Time series of the ratio of total tropospheric NO₂ vertical column to clear-sky tropospheric NO₂ vertical column retrieved using the OCRA/ROCINN and FRESCO v7 cloud products for GOME-2A over Europe.

Table 3-4: Selected settings for forward model parameters used in the calculation of tropospheric NO₂ AMFs in the ESA CCI ECV Precursor project for the morning sensors.

Forward model parameter	GOME	SCIAMACHY	GOME-2A	GOME-2B	GOME-2C
Surface albedo	GOME-2 DLER v4 MIN	GOME-2 DLER v4 MIN	GOME-2 DLER v4 MIN	GOME-2 DLER v4 MIN	GOME-2 DLER v4 MIN
Surface pressure	ECMWF/DEM	ECMWF/DEM	GTOPO30	GTOPO30	GTOPO30
Cloud fraction	FRESCO v7/v8	FRESCO v7/v8	OCRA	OCRA	OCRA
Cloud pressure	FRESCO v7/v8	FRESCO v7/v8	ROCINN	ROCINN	ROCINN
Cloud albedo	0.8	0.8	ROCINN	ROCINN	ROCINN
A priori NO ₂ profile	TM5-MP	TM5-MP	TM5-MP/CAMS	TM5-MP/CAMS	TM5-MP/CAMS

Table 3-5 summarizes the selection of information sources for ancillary data (or forward model parameters) on the atmospheric state needed for each pixel to calculate the tropospheric AMF M_{tr} via the recipe of Eq. 3-2 - Eq. 3-5 above for OMI and TROPOMI. For OMI, several changes have been made relative to the OMI QA4ECV approach, mostly to make the OMI NO₂ retrieval as consistent as possible with the operational TROPOMI retrieval. This includes the cloud fraction and cloud radiance fraction now taken from the NO₂ spectral window at 440 nm instead of O₂-O₂ continuum near 477 nm. A notable but unavoidable difference, however, is that for OMI, cloud pressures are retrieved from the O₂-O₂ absorption signature, which has proved to be less sensitive to low clouds than FRESCO.

One innovative aspect in the OMI and TROPOMI NO₂ retrievals that will be used in the ESA CCI ECV Precursor project is that the cloud products used provide (1) an effective cloud fraction





and cloud pressure, but also (2) a scene albedo and scene pressure assuming that the cloud fraction is zero. When snow/ice flags, or sunglint flags are up, option (2) may be selected to calculate the AMF and ultimate tropospheric column. For example, if the scene pressure retrieved for a pixel is close to the reported ECMWF surface pressure, the scene is often brighter than indicated by the surface albedo climatology, because of sudden snowfall, or sunglint. Riess et al. (2022) showed that accurate tropospheric AMFs can be calculated with a cloud fraction of zero, and a surface albedo and effective surface pressure retrieved by the cloud retrieval.

Table 3-5: Selected settings for forward model parameters used in the calculation of tropospheric NO₂ AMFs in the ESA CCI ECV Precursor project for the afternoon sensors.

Forward model parameter	OMI	TROPOMI
Surface albedo	OMI LER MIN	S5P DLER MIN
Surface pressure	ECMWF/DEM	ECMWF/DEM
Cloud fraction	NO ₂ fitting window	NO ₂ fitting window
Cloud pressure	O ₂ -O ₂	FRESCO-wide
Cloud albedo	0.8	0.8
A priori NO ₂ profile	TM5-MP	TM5-MP

3.1.6. Information content and uncertainty estimate

Table 3-6 summarizes the assessment of the main contributions to the overall uncertainty budget on tropospheric NO₂ retrieval within this project. These uncertainties should be interpreted as representative of typical single-pixel uncertainties for retrievals over polluted regions encountered by users. Expressions for systematic or structural uncertainty are under investigation and will be provided in cycle 2 of the project.





Table 3-6: Estimation of the uncertainty contributions to the overall, per-pixel tropospheric NO₂ column uncertainty over polluted regions.

Uncertainty contribution	Random	Systematic
From NO ₂ slant column ($\frac{\sigma_{N_s}}{M_{tr}}$)	0.4-0.8×10 ¹⁵ molec. cm ⁻²	< 1.0×10 ¹⁵ molec. cm ⁻²
From stratosphere ($\frac{\sigma_{N_s, strat}}{M_{tr}}$)	0.2×10 ¹⁵ molec. cm ⁻²	< 0.5×10 ¹⁵ molec. cm ⁻²
From tropospheric AMF ($\frac{\sigma_{N_s}}{M_{tr}}$)	20-35% (sensor dependent)	TBD
Approximation for σ_{N_v}	$\sigma_{N_v} = 0.5 \times 10^{15} + 0.3N_v$	TBD



3.2. Formaldehyde (L2-HCHO)

We provide here only a short description of the L2 HCHO DOAS retrieval. Extended descriptions are provided in De Smedt et al. (2018) (QA4ECV), De Smedt et al. (2021) (TROPOMI) and Valks et al. (2019) (GOME-2 AC SAF). Within the CCI+ ozone precursors project, the settings of the L2 retrieval algorithm have been updated with the aim to further improve the consistency between the sensors and to include the more recent auxiliary datasets. The settings for each step of the algorithm and for each sensor are summarized in sections 3.2.2, 3.2.3 and 0, and in the corresponding tables.

3.2.1. Flow diagram of the L2 retrieval algorithm

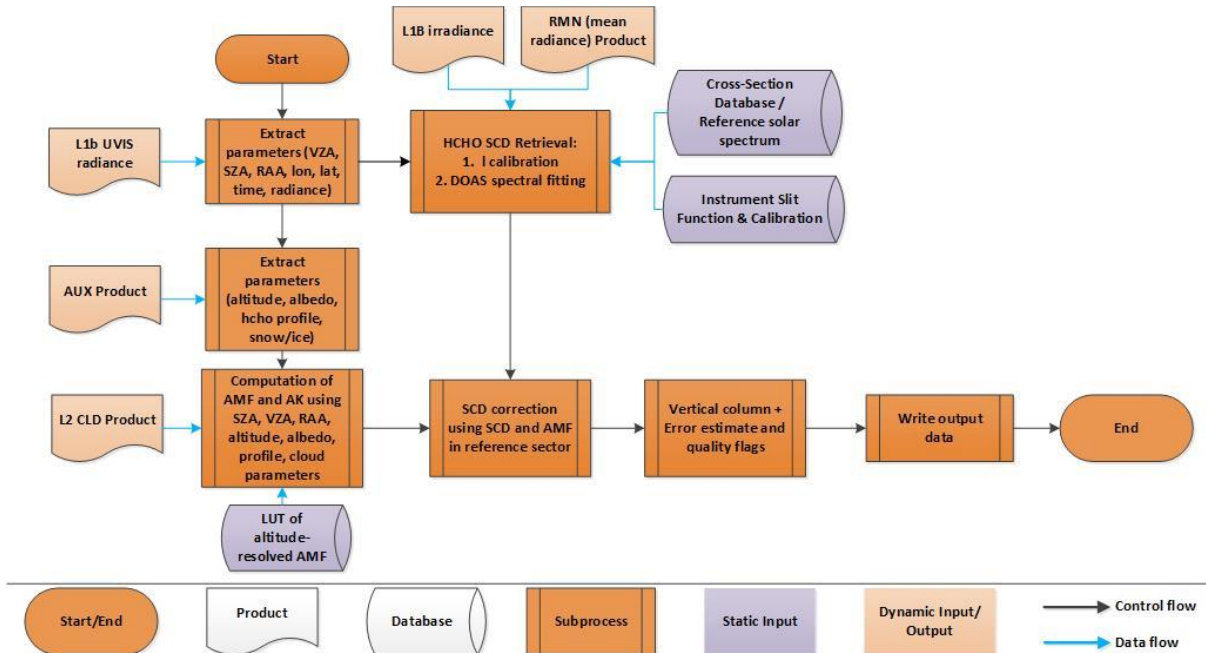


Figure 3-4: Flow Diagram of the DOAS retrieval algorithm for HCHO.

Figure 3-4 shows the flow diagram of the L2 HCHO DOAS retrieval algorithm. The HCHO slant column (N_s) fit is performed in the UV, and the relevant absorption cross-section data as well as instrumental characteristics are used as input. An average of radiances selected in a remote sector is calculated to obtain a reference spectrum for the DOAS fit. Subsequently, to convert the slant column to a vertical column (N_v), an air mass factor (M) that accounts for the average light path through the atmosphere is calculated. For this purpose, several auxiliary data are read from external sources: cloud cover data, topographic information, surface albedo, and the a priori shape of the vertical HCHO profile in the atmosphere. Additional background normalization is required in the case of weak absorbers such as formaldehyde. Before converting the slant columns N_s into vertical columns N_v , remote background values of N_s are normalized to compensate for unknown offsets ($N_{s,0}$), and background vertical columns derived from a CTM is added ($N_{v,0}$).



The final HCHO vertical column (N_v) is obtained using the following equation:

$$N_v = \frac{N_s - \overline{N_{s,0}}}{M} + \overline{N_{v,0}} = \frac{N_s - \overline{N_{s,0}} + \overline{M_0} \times \overline{N_{v,0,CTM}}}{M} \quad \text{Eq. 3-6}$$

The main outputs of the different steps of algorithm are:

1. The slant column density (N_s): see section 3.2.2.
2. The air mass factor (M): see section 3.2.3.
3. The mean values used for the reference sector correction ($\overline{N_{s,0}}$, $\overline{N_{v,0,CTM}}$, and $\overline{M_0}$): see section 0.

Complementary product information includes the averaging kernel, the error on the total column, and quality assurance values.

3.2.2. Slant Columns

The fit of the slant columns (N_s) is performed in the UV part of the spectra (see Table 3-7 for details). All cross sections are convolved with the instrumental slit functions (for every row separately for OMI and TROPOMI). The TROPOMI slit functions have been adjusted once after launch and the cross-sections have been pre-convolved. For OMI, GOME-2, SCIAMACHY and GOME, the slit functions are adjusted daily and the cross sections are convolved online. The DOAS reference spectrum is updated daily with an average of Earth radiances measured in the equatorial Pacific region. The fit therefore results in a differential slant column, corresponding to the HCHO excess over sources compared to the remote background. Details are provided in Table 3-7.

Table 3-7: Settings used for DOAS spectral fitting for the different satellite instruments.

Sensor / Settings	TROPOMI	OMI	GOME-2	SCIAMACHY	GOME
Level 1 version	Collection 3	OML1BRUG.003	R 5.12	Y 8.02	5.1
Wavelength calibration	325-360 nm Pre convolution with adjusted FM IRSF, per row	325-360 nm Online convolution with adjusted slit function from PFM IRSF, per row	325-360 nm Online convolution with adjusted slit function from PFM IRSF	325-360 nm Fit of the slit function: Gaussian line shape	
Solar Atlas	Chance and Kurucz, 2010				
Fitting intervals	328.5-359 nm				328.5-346 nm
Reference spectrum	Daily average of radiances, per detector row.		Daily average of radiances, per VZA bins.		Daily average of radiances, per pixel type (0,1,2,3).
Reference sector	Lat: [-5° 5°], Long: [180° 240°]	Lat: [-15° 15°], Long: [150° 250°]			
Cross-sections	HCHO: Meller and Moortgat (2000), 298K O ₃ : Serdyuchenko et al. (2013), 223 + 243K NO ₂ : Vandaele et al. (1998), 220K BrO: Fleischmann et al. (2004), 223K O ₄ : Thalman et al., 2013, 293K Ring: Generated following Chance et al, 1997.				



	Non linear O ₃ terms: generated internally based on O3223. Calculated from the Taylor expansion of the wavelength and the O3 optical depth (Puķīte et al., 2010).		
Additional cross-sections		Polarisation_eta, polarisation_zeta, Pseudo_east_west	undersampling
Polynomial	Order 5		
Intensity offset	Linear offset (1/reference spectrum)		
Shift / stretch	Non-linear / First order		
Iterative Spike Removal	Tolerance factor 5, maximum iteration 3		Tolerance factor 3, maximum iteration 3

3.2.3. Air Mass Factors

For optically thin absorbers, the tropospheric AMF (M) can be expressed as the sum of the altitude dependent air mass factors (m_l) weighted by the partial columns (n_{al}) of the a priori vertical profile in each vertical layer l , from the surface up to the tropopause index (lt) (Palmer et al., 2001):

$$M = \frac{\sum_{l=1}^{lt} m_l(\lambda, \theta_0, \theta, \varphi, A_s, p_s, f_c, A_{cloud}, p_{cloud}) n_{al}(lat, long, time)}{\sum_{l=1}^{lt} n_{al}(lat, long, time)} \quad \text{Eq. 3-7}$$

where A_s is the surface albedo, p_s is the surface pressure, while f_c , A_{cloud} and p_{cloud} are respectively the cloud fraction, cloud albedo and cloud pressure. The AMF calculation assumes Lambertian reflectors for the ground and the clouds and makes use of pre-calculated altitude dependent air mass factors look-up-tables. This look up table has been created using the VLIDORT 2.6 radiative transfer model (Spurr et al., 2008a) at a 340 nm, wavelength representative for the retrieval interval. For each pixel, m_l is computed by linear interpolation of the LUT at the a-priori profile pressure grid and using the auxiliary data sets described in Table 3-8. The AMF calculation module is almost identical to the one used for the operational retrieval of HCHO columns from TROPOMI, and the reader is referred to the S5P HCHO ATBD for more detailed information (De Smedt et al., 2018, 2021).

Table 3-8: Input used for AMF calculation for the different satellite instruments.

Sensor / Settings	TROPOMI	OMI	GOME-2	SCIAMACHY	GOME
Surface albedo	TBD: OMI min LER (Kleipool et al., 2008) or TROPOMI DLER v2 (Tilstra, 2023)		TBD: GOME-2 DLER v4 (Tilstra et al., 2021), OMI min LER (Kleipool et al., 2008) or TROPOMI DLER v2 (Tilstra et al., 2023)		
Cloud product	OCRA-ROCINN collect. 3	OMCLDO2 v2.0	AC SAF OCRA-ROCINN	FRESCO version SC-v7	FRESCO version GO-v7
Cloud correction	Baseline: cloud filtering, no cloud correction (VCD clear, AMF clear, AK clear). Optional: cloud correction based on the independent pixel approximation and a Lambertian reflector cloud model, no cloud correction for CF <5% (CF=0) (VCD, AMF, AK).				
A priori profiles	CAMS reanalysis, 3h time step				TBD: CAMS reanalysis, 3h time step, climatology or control run.





SI treatment	TBD
--------------	-----

3.2.4. Background correction

Retrieved HCHO slant columns can present large offsets depending on minor changes in the fit settings and minor instrumental spectral inaccuracies. Resulting offsets are generally global but also show particular dependencies, mainly with detector row or VZA (across track) and with latitude (along track). Offsets can also present a time dependency, resulting from instrumental degradation. The background correction is based on the assumption that the HCHO column observed over remote oceanic regions (Pacific Ocean) is only due to methane oxidation. The natural background level of HCHO is well estimated from chemistry model simulations of CH₄ oxidation.

The correction includes two steps:

1. a destriping correction in the Equatorial Pacific (reference sector 1, dimension: ground pixels/SZA bins). Offset correction factors are determined for each ground pixel or SZA bin as the median of all slant columns ($N_{s,0}$) falling into to the Equatorial Pacific. Data selection is based on the residuals from the DOAS fit and on the cloud fraction.
2. a latitudinal-bias correction in the entire Pacific Ocean (reference sector 2, dimension: latitude bins). The second correction relies on latitude-dependant polynomials, calculated using the destriped slant columns averaged in latitude bins in the entire Pacific Ocean, independently of their cross-track position. An additional data selection, based on the destriped slant column value in the reference sector is applied in order to exclude grid cells with real emissions (ex: from Alaska fires).

At the end of these steps, the correction factors are subtracted from all SCDs (N_s) of all observations worldwide, so that in the reference sector, the median background corrected slant columns are close to zero. To the corrected HCHO slant columns, the background HCHO columns from the model are added (see equation 3-6).

In practice, the corrections are calculated using 2-dimensional arrays (dimension: latitude bins x ground pixels/SZA bins) updated on a daily basis and providing the median values of the observations falling into the entire reference sector (reference sector 2) for the following variables:

- $\overline{N_{s,0}}$: mean HCHO slant column density in the reference sector.
- $\overline{M_0}$: mean clear air mass factor in the reference sector.
- $\overline{N_{v,0,CTM}}$: mean model HCHO vertical in the reference sector. The model columns are derived from the a priori profiles.

Details of the reference sector limits, array dimensions and selection criteria are provided in Table 3-9.



Table 3-9: Background correction settings for the different satellite instruments. To be updated.

Sensor / Settings	TROPOMI	OMI	GOME-2	SCIAMACHY	GOME
reference sector 1	Lat: [-15° 15°], Long: [150° 250°]				
reference sector 2	Lat: [-90° 90°] Long: [150° 250°]				
Acrosstrack dim. in ref. sector 1	450 ground pixels	60 ground pixels	SZA bins: TBD	SZA bins: TBD	3 pixel types (east, center, west)
Along track dim. in ref. sector 2	36 (5° latitude bin)				
RMS threshold	$3RMS$				
CF threshold	0.5				
SZA threshold	70				
Threshold of the destriped SCD for applying the zonal correction	2.5e16				
Latitudinal normalization polynomial degree	8				
Minimum number of reference SCDs	50	TBD	TBD	TBD	TBD

3.2.5. Error estimate

Many factors contribute to the retrieved HCHO tropospheric column uncertainty. The random uncertainty of the final HCHO columns is dominated by the error of the fitted slant columns (instrument dependent). The systematic uncertainty is dominated by error in air mass factor calculations, resulting from uncertainties on a priori information such as a priori profile shapes, clouds or surface albedo (mostly not instrument dependent). We refer to the End-to-End ECV Uncertainty Budget (E3UB) document for a detailed description of the implementation of error modules in the L2 retrievals and an analysis of the error budget for HCHO.



3.3. Sulfur dioxide (L2-SO₂)

3.3.1. Overview

The SO₂ algorithm relies on the two steps Covariance-Based Retrieval Algorithm (COBRA; Theys et al., 2021) to retrieve sulphur dioxide vertical columns from satellite nadir UV hyperspectral measurements. First, the measured top-of-atmosphere radiances are analyzed and yield the slant columns (SCD, or the integrated concentration along the light path). In a second step, a radiative transfer calculation of air mass factors (AMF) is performed to convert the SCD into the VCD output (VCD=SCD/AMF). A diagram illustrating the algorithm modules is given in Figure 3-5.

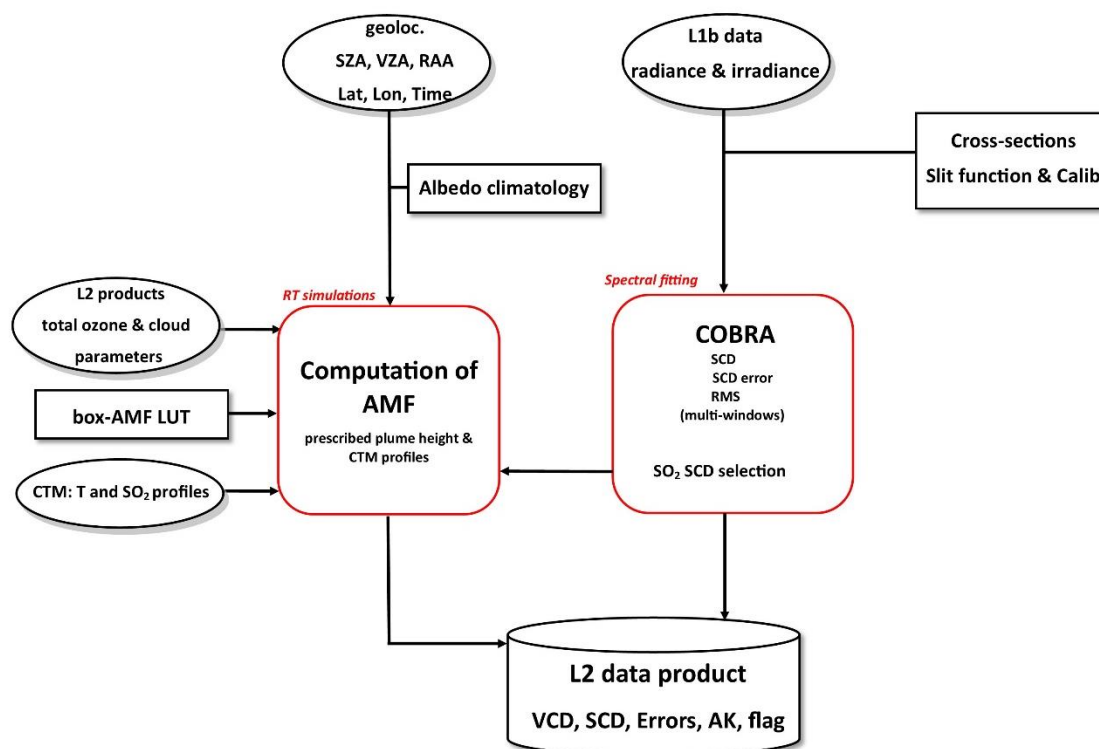


Figure 3-5: Flow diagram of the SO₂ column retrieval algorithm.

The radiance and irradiance data are read from the L1b files, along with geolocation data as pixel coordinates and observation geometry. The relevant absorption cross sections data as well as characteristics of the instrument like slit function and wavelength calibration parameters are used as input of the spectral fitting module. The SO₂ fit is performed using COBRA in multiple fitting windows, characterized by different SO₂ absorption strengths. Depending on the retrieved columns amounts in the different fitting windows, a selection of the final SCD is performed. This step is to avoid saturation, ensuring that the results are valid for a wide range of SO₂ column amount. Subsequently, the slant column is converted to a



vertical column through division by an air mass factor which accounts for the average light path through the atmosphere. To do so, altitude-resolved air mass factors are extracted from a pre-computed look-up-table. The AMF is computed for SO₂ profiles from a chemical transport model as well as for box profiles with prescribed SO₂ plume heights, representative of volcanic scenarios. The AMF module also includes calculation of errors and column averaging kernels. Note that the AMF module is similar to the one used for TROPOMI operational SO₂ retrievals (Theys et al., 2017, 2023).

The next subsections give details on the two algorithmic steps (spectral fitting and radiative transfer calculations), as well as an overview of the input data needed for the retrievals.

3.3.2. Algorithm description

Spectral fitting

In a preparatory step, we extract the intensities over the wavelength range 310-390 nm and compute the total measured optical depth $y = -\log(I/I_0)$, which is the logarithmic ratio of the wavelength calibrated measured intensity (I) and the solar intensity spectrum (I_0). For the wavelength calibration, we use the same approach as for the TROPOMI operational SO₂ algorithm (as described in Theys et al., 2017), although the exact settings depend on the satellite instrument considered.

We assume the measurement vector (y) can be linearized around a background SO₂-free spectrum \bar{y} :

$$y = \bar{y} + k \cdot SCD + \epsilon_{bg} + \epsilon \quad \text{Eq. 3-8}$$

with ϵ_{bg} being the uncertainty on the SO₂-free spectrum, and ϵ is the measurement noise. The SO₂ contribution to the measured spectral optical depth is the product of the instrument slit convolved absorption cross-section vector k and the SO₂ slant column density SCD (in molecules/cm²).

The basic principle of the method is to consider all contributions to the difference ($y - \bar{y}$) other than SO₂ as an error term ($\epsilon_{bg} + \epsilon$) with a Gaussian distribution. If one can define an ensemble Y of N measured spectra, representative of the total ($\epsilon_{bg} + \epsilon$) variability, and characterized by a mean measurement vector \bar{y} and a covariance matrix S :

$$S = \frac{1}{N-1} \cdot \sum_{i=1}^N (y_i - \bar{y})(y_i - \bar{y})^T \quad \text{Eq. 3-9}$$

then the solution of the problem writes as:

$$\widehat{SCD} = (k^T S^{-1} k)^{-1} k^T S^{-1} (y - \bar{y}) \quad \text{Eq. 3-10}$$





It follows that the retrieval error on the SCD is given by:

$$\widehat{SCD}_{err} = \chi \cdot \sqrt{(k^T S^{-1} k)^{-1}} \quad \text{Eq. 3-11}$$

with χ being the normalized root-mean-square, i.e.:

$$\chi^2 = \frac{1}{N_\lambda - 1} \cdot (\Delta y^T S^{-1} \Delta y) \quad \text{Eq. 3-12}$$

where $\Delta y = y - \bar{y} - k \cdot \widehat{SCD}$ (residual) and N_λ being the number of wavelengths in the fitting interval. This variable evaluates the fit quality and is typically close to 1, except for conditions of bad fit quality ($\chi \gg 1$).

Fundamentally, COBRA generalizes the measurement error covariance matrix used in Optimal Estimation Methods (OEM; Rodgers, 2000) by incorporating geophysical background spectral variability (including all cross-correlations), variability from the atmosphere or induced by instrumental changes. A remarkable feature of COBRA is its simplicity. The SCD retrieval in Eq. 3-10 reduces to a simple dot product between the $y - \bar{y}$ residue and $k^T S^{-1}$ (skipping the normalization factor $(k^T S^{-1} k)^{-1}$); the target SCD is only the fit parameter, this is contrast to most other retrieval methods. Note that, in principle, the COBRA approach is applicable to any spectral fitting range. Here, the SO₂ SCD retrieval is performed in different fitting windows. There are differences depending on the satellite instrument used but, as a baseline, SCDs are typically retrieved from 310.5-326 nm (w1), 325-335 nm (w2) and 360-390 nm (w3). In the following, the slant column results in the respective windows are referred as SCD_i (i=1,2,3). It should be noted that, in practice, a covariance matrix S (and mean spectrum \bar{y}) is associated specifically to each window, but the set of clean spectra Y used to construct the covariance matrices is common to all fitting windows.

Although simple in concept, the practical implementation for COBRA requires some caution. The main difficulty lies in the definition of the ensemble Y used to construct S . The reader is referred to Theys et al. (2021) for more detailed discussion on COBRA pro and cons. For the retrieval of SO₂, we have conducted several tests and come to the following general implementation choices (note that the settings are different for each sensor, see Table 3.1): the input spectra for the covariance matrix calculation are analyzed separately for each across-track position. We also treat each orbit/day individually. The data are first screened for solar zenith angles larger than 65°, and to cope with the latitudinal dependence, the data are divided into a number (from 3 to 6) of equal and non-overlapping along-track segments. For each segment, an initial covariance matrix S is derived for w1 (the most sensitive spectral range) and initial estimates of SO₂ slant columns (SCD1) are inverted through Eq. 3-10. To do so, the spectra with strong SO₂ absorption must be filtered out to avoid contamination of the initial covariance matrix. For this purpose, SO₂ SCD results from a simplified DOAS sub-module are used (see Table 3-10). In a second step, improved estimates of S and SO₂ SCDs are obtained



iteratively by further removing SO₂ contaminated spectra from the ensemble Y. For this, we use the ratio of the SCD to its retrieval uncertainty (Eq. 3-10 and Eq. 3-11), referred to as the signal to noise ratio (SNR). A fixed SNR upper value of 1.5 is used for the filtering and the number of iterations is set to 5. Note that most pixels are SO₂-free, except in some rare cases of extended SO₂ plumes. A lower limit on the number N of SO₂-free spectra is set to 50. If this limit is reached, because of a major volcanic eruption for example, the SO₂ SCD retrieval for the corresponding across-track position–segment pair falls back on the SCDs from the last iteration or ultimately the DOAS SCD results.

Table 3-10: Settings used for COBRA spectral fitting for the different satellite instruments used (preliminary).

	Satellite instrument			
	GOME/ERS2	SCIAMACHY/ ENVISAT	OMI/AURA	TROPOMI/S5P
Fitting intervals	313-326, 325-335nm	tbd	310.5-325, 325-335, 360-390 nm	310.5-325, 325-335, 360-390 nm
Covariance calculation	per day, per viewing angle (3), 3 segments	tbd	per orbit, per row (60), 3 segments*	per orbit, per row (450), 6 segments
DOAS pre-filtering	no	tbd	yes, from linear DOAS module. SCD1 _{doas} <5DU & SCD2 _{doas} <15DU	yes, from operational product. SCD1 _{doas} <2DU & SCD2 _{doas} <30DU (**)
Cross-sections†	SO ₂ : <i>Bogumil et al.</i> , 2003 (203K) for w1 & w2, <i>Hermans et al.</i> (2009, extrapolated at 203K) for w3. Other cross-sections and settings used in DOAS retrievals: see <i>Theys et al.</i> , 2017, 2023. For linear DOAS module: irradiance used as reference, fit of wavelength shift and squeeze according to <i>Beirle et al.</i> (2013), no SCD background correction.			

*Pixels affected by the row anomaly are filtered out. ** For rows 23-430. External rows: 3 DU, 40 DU, respectively.
† All cross-sections are convolved using instrumental spectral response functions (row dependent in case of OMI and TROPOMI). Note: DU=Dosbon Unit (1 DU: 2.69x10¹⁶ molecules/cm²).

The output results of the spectral fitting procedure described above, are SO₂ slant columns in three fitting windows (SCD1, SCD2 and SCD3). The next step is to combine the slant columns into a single SCD. For this, a set of transition criteria are used that are based on the measured SO₂ SCDs. The latter are summarized in Table 3-11.

Table 3-11: Criteria for selecting alternative fitting windows.

Window number	w1	w2	w3
Wavelength range	310.5 – 326 nm	325-335 nm	360-390 nm
Derived slant column	SCD1	SCD2	SCD3
Application	Baseline	SCD1 > 5 DU & SCD2 > 30 DU &	w2 selected & SCD3 > 100 DU &



		SCD2 > 2 x SCD1	SCD3 > 2 x SCD2
--	--	-----------------	-----------------

Radiative transfer calculations

The AMF simulates the trace gas concentration integrated along the complex photon path in the atmosphere, relative to the vertical path. Here, the AMF can be formulated (Palmer et al., 2001) by:

$$AMF = \int m'(p) \cdot s(p) dp \quad \text{Eq. 3-13}$$

with $m'=m(p)/C_{temp}(p)$, where $m(p)$ is the so-called weighting function (WF) or pressure dependent air mass factor, C_{temp} is a temperature correction and s is the SO₂ normalized a-priori mixing ratio profile, as function of pressure (p).

The AMF calculation assumes Lambertian reflectors for the ground and the clouds and makes use of pre-calculated WF look-up-tables at suitable wavelengths (depending on the fitting window used). We note that the AMF calculation module is almost identical to the one used for the operational retrieval of SO₂ columns from TROPOMI, and the reader is referred to the S5P SO₂ ATBD for more detailed information (Theys et al., 2017, 2023). Here we limit the description to the differences compared to the operational S5P AMF calculation module.

In practice, the WF depends on observation geometry (solar zenith angle: SZA, line-of-sight angle: LOS, relative azimuth angle: RAA), total ozone column (TO3), scene albedo (alb), surface pressure (p_s), cloud top pressure (p_{cloud}) and effective cloud fraction (f_{eff}). The generation of the WF LUT has been done for a large range of physical parameters (as listed in Table 4 of Theys et al., 2017). For each pixel, the WF is computed by linear interpolation of the WF LUT at the a-priori profile pressure grid and using the auxiliary data sets described in Table 3-12. Finally, the AMF is calculated using Eq. 3-13.

Table 3-12: Input parameters used for AMF calculation and the for the different satellite instruments used (preliminary).

	Satellite instrument			
	GOME/ERS2	SCIAMACHY/ ENVISAT	OMI/AURA	TROPOMI/S5P
Total ozone column	tbd / CCI TO3 product	tbd / CCI TO3 product	OMSO2.003	S5P L2 SO ₂ OFL+RPRO
Surface albedo*	OMI minLER 328, 376 nm (Kleipool et al., 2008)	OMI minLER 328, 376 nm (Kleipool et al., 2008)	OMI minLER 328, 376 nm (Kleipool et al., 2008)	OMI/TROPOMI minLER 328, 376 nm (Kleipool et al., 2008 ; Tilstra, 2023)
Clouds** (product/cloud correction)	FRESCOv7 (Wang et al., 2008)/no	tbd/no	OMCLDO2.003/no	OCRA-ROCINN (from S5P L2 SO ₂ OFL+RPRO v3.2)/no
SO₂ profile shapes and temperature profiles	CAMSrea/TM5 (tbd) +box profiles at 1,7,15km height	CAMSrea/TM5 (tbd) +box profiles at 1,7,15km height	CAMSrea/TM5 (tbd) +box profiles at 1,7,15km height	CAMSrea/TM5 (tbd) +box profiles at 1,7,15km height



* Current baseline is to process only the scenes free of snow/ice (identified as such by a proper snow/ice flag).
** Cloud correction applied or not applied: total AMF or clear-sky AMF are used in the VCD calculation.

3.3.3. Information content and uncertainty estimate

Because exploiting the information content of the L2_SO₂ product is first a matter of data filtering, it requires some caution. To describe the quality of the retrieved SO₂ vertical column (and guide the users), a quality assurance value (qa_value) is assigned to each pixel. The quality assurance value is a numerical value with a range of [0 1], with the convention that a value <0.5 means that the pixel retrieval results should be discarded. The initial qa_value is 1 (full quality). For some conditions (e.g., in the presence of clouds) or when an error/warning flag is raised, the qa_value is reduced by a certain fraction. As a matter of fact, the qa_value calculation rule is instrument specific and, at the time of writing, it is not fully defined. In a next ATBD version, the calculation rule will be described in more detail but as a general rule, good quality results (qa_value>0.5) can only be obtained if all of the following conditions are fulfilled: AMF>0.15, -3.5 DU<VCD<10 DU, SZA<65, cloud fraction<0.3.

It should be emphasized that qa_value for SO₂ is only applicable to the VCD for the pollution scenario (based on model a-priori profiles). For volcanic cases, the retrievals are not as difficult as for boundary layer SO₂, especially for volcanic plumes above clouds, and it is difficult to assign a general quality flag for these cases. It is suggested that the users consider the SO₂ VCD assuming box profiles for volcanic cases.

Regarding the total uncertainty characterization, it is the subject of a different document (End-to-End ECV Uncertainty Budget). Table 3-13 summarizes the assessment of the main contributions to the global error budget on SO₂ retrieval from COBRA.

Table 3-13: Estimation of the error sources of the SO₂ COBRA retrieval (preliminary) for typical polluted conditions, at low/high SZA (latitudes). Blue and red fields indicate random (precision) and systematic (trueness) errors. Total errors are computed assuming all contributions are mutually uncorrelated.

Error source	Error on VCD	
	SZA=30°	SZA=60°
Instrument signal-to-noise	0.6 DU	1.2 DU
SO ₂ absorption cross-section, spectral interferences +instrumental features	0.1 DU + 10%	0.2 DU + 15%
Surface albedo*	15%	15%
SO ₂ Profile shape	20-50%	20-50%
Cloud correction	10%	10%
Cloud fraction	5%	5%
Cloud pressure	20%	20%
Aerosols (except in case of volcanic eruptions)	< 15%	< 25%
Structural (AMF)	15%	15%
Total random error	0.6 DU + 20%	1.2 DU + 20%





Total systematic error	0.1 DU + 45%	0.2 DU + 55 %
Total systematic error kernel	0.1 DU + 27%	0.2 DU + 35 %

*snow/ice free scenes



3.4. Glyoxal (L2-CHOCHO)

3.4.1. Overview

The glyoxal vertical column retrieval is based on the differential optical absorption spectroscopy (DOAS) algorithm for TROPOMI by Lerot et al. (2021) presented in Figure 3-6, and has been transferred to the OMI and GOME-2 instruments to obtain maximally consistent results from all sensors.

As a first step, the measured optical depth at top of atmosphere is fit against a set of known absorption spectra for glyoxal and other important absorbers in the same wavelength range, as well as pseudo absorbers which compensate for instrumental effects, in order to determine the glyoxal column density along the effective light path, or slant column density (SCD). In the next step, we divide the SCD by an air mass factor (AMF) in order to obtain a vertical column density (VCD). The AMF is calculated by modelling the radiative transfer through the atmosphere, considering each observation's viewing geometry and local surface albedo, for a model atmosphere based on an a priori vertical profile shape from a chemical transport model. An empirical correction is applied to the retrieved vertical columns to compensate for the effect of strong NO₂ absorption on the spectral fit. A final background correction to the resulting VCD's is compensates for systematic differences which arise from instrument calibration imperfections and viewing zenith angle (VZA) dependencies.

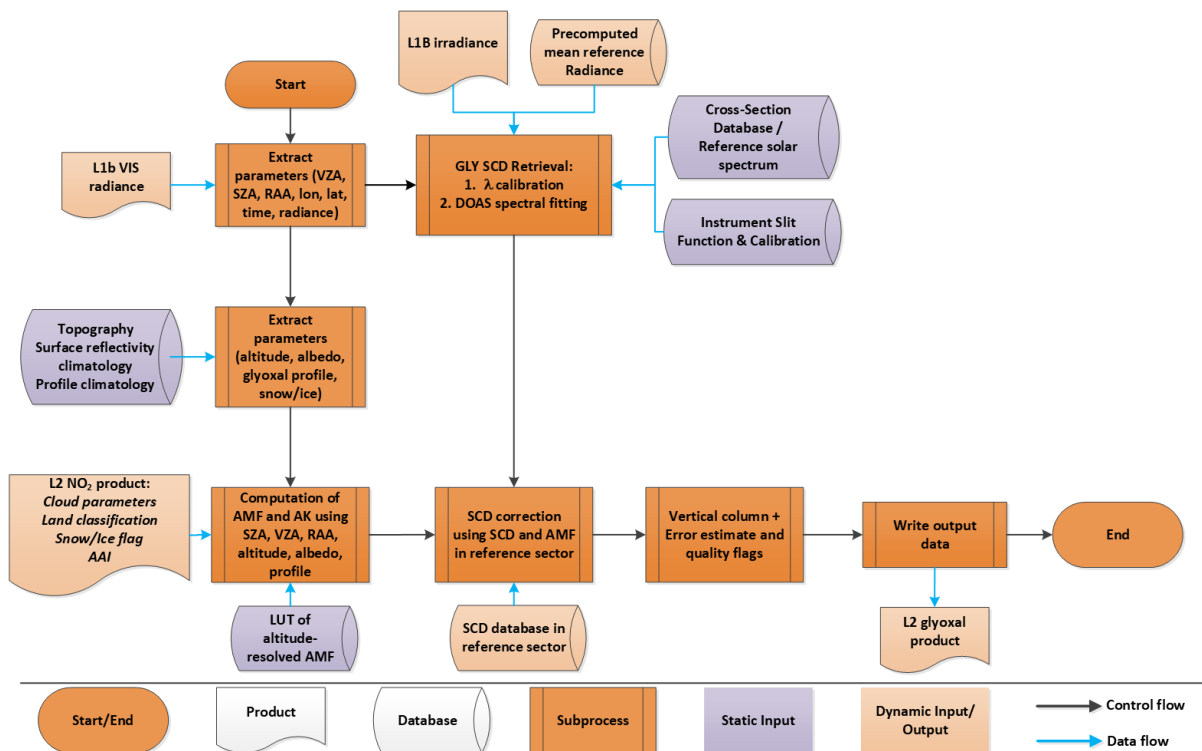


Figure 3-6: Glyoxal retrieval flowchart



3.4.2. Algorithm description

Spectral fitting

In order to minimize the effect of spectral interferences and instrumental limitations, the reference spectrum I_0 used in the DOAS fit for glyoxal is a daily mean radiance spectrum obtained from measurements over a region in the equatorial Pacific (typically 15°S -15°N and 150°-250°E, where the exact settings differ per instrument, see Table 3-14). A calibration procedure (Lerot et al., 2021; Danckaert et al., 2017) ensures that this reference spectrum is aligned with the wavelength grid of the cross sections used in the fit. For each observed radiance I , we then fit the atmospheric transmittance spectrum in a wavelength range of 435-460 nm, which includes the strongest glyoxal absorption bands, and has been found to work well for glyoxal retrievals for all 3 instruments (Barkley et al., 2017; Lerot et al., 2010; Alvarado et al., 2014; Chan Miller et al., 2014). A non-linear fitting procedure (Danckaert et al., 2017) is used to align the wavelength grid of the radiance I with that of the calibrated reference I_0 . We then fit the optical depth against a set of cross sections σ_j and obtain slant column densities $N_{s,j}$ from the linear least squares solution of the following equation:

$$\ln \frac{I}{I_0}(\lambda) = \sum_j \sigma_j(\lambda) N_{s,j} + P(\lambda) + \epsilon \quad \text{Eq. 3-14}$$

Here, the set of cross sections σ_j includes absorption spectra for glyoxal, O₃, NO₂ (at 220K and 294K to account for temperature dependence), O₂ – O₂ and water vapour. Absorption spectra are obtained from laboratory measurements and convolved to instrument resolution using the available data on the respective instrument spectral response function; see Table 3-15 for an overview. Additional cross sections are included to treat the effect of inelastic scattering (Ring effect) and intensity offsets in the spectra such as those caused by instrumental stray light. For the GOME-2 instruments, additional cross sections are included to compensate for polarization effects. For TROPOMI, a set of cross sections based on mean residual spectra is added to compensate for the effect of scene intensity heterogeneity (Richter, 2018). A polynomial $P(\lambda)$ of degree 3 is included to fit broad-band atmospheric absorption features.

Table 3-14: Selected pacific background region for daily reference radiance per instrument.

Instrument	Radiance reference region
TROPOMI	15°S – 15°N, 180°E – 240°E
OMI	15°S – 15°N, 150°E – 250°E
GOME-2 / METOP-A/B	15°S – 15°N, 180°E – 240°E
GOME-2 / METOP-C	20°S – 20°N, 150°E – 250°E

Table 3-15: Absorption cross sections

Species	Cross section
Glyoxal	Volkamer et al. (2005)
O ₃	Serdyuchenko et al. (2014), 223K
NO ₂	Vandaele et al. (1998), 220K and 294K



O₂ – O₂	Thalman and Volkamer (2013), 293K
H₂O (water vapour)	Rothman et al. (2013), 293K

Radiative transfer calculations

To compute the AMF, we rely on the formulation from (Palmer et al., 2001), which decouples the radiative transfer computation from the absorber's a priori atmospheric profile shape:

$$AMF = \sum_{j=1}^N m_j s_j \quad \text{Eq. 3-15}$$

Where the atmosphere has been discretized into N vertical layers, m_j is the box air-mass factor or weighting function for layer j , and $s_j = \frac{n_j}{\sum_k n_k}$ is the a priori profile shape.

For the glyoxal AMF computation, we use a precomputed five dimensional lookup table of box air mass factors $m_j(\theta_0, \theta, \phi, A, p_s)$, depending on the solar zenith angle θ_0 , the line-of-sight zenith angle θ , relative azimuth angle ϕ , surface albedo A and surface pressure p_s , computed at a wavelength of 448nm using the VLIDORT 2.7 radiative transfer code (Lerot et al., 2021). For the retrieval, this lookup table is interpolated using the observation geometry values provided in the L1B input data, surface albedo from the OMI min LER albedo product (Kleipool et al. 2008), and scene surface pressure (Table 3-16). Profile shapes s are obtained by interpolating a database of monthly a priori profiles for morning and noon overpass times generated by the chemical transport model MAGRITTE on a $1^\circ \times 1^\circ$ longitude/latitude grid. For observations over oceans, we use a fixed glyoxal concentration profile measured with an airborne MAX-DOAS instrument over the Pacific Ocean during the TORERO campaign (Volkamer et al., 2015), as current models cannot reproduce the enhanced glyoxal concentrations which have been detected over oceans in several studies. Table 3-16 provides an overview of the exact input data sets used for each sensor.

The effects of clouds and aerosol are not modeled. Instead, we apply a strict filter where all observations with an effective cloud fraction above 20% are discarded. This is motivated by the fact that glyoxal slant columns over bright scenes tend to be biased high, due to poorly understood residual spectral interferences. For the same reason, observations over scenes with snow and ice are excluded from the retrieval. Observations with solar zenith angle above 70° are also excluded from the retrieval, motivated by the fact that, especially at low sun elevation, Rayleigh scattering strongly reduces the sensitivity of nadir-viewing UV-visible instruments to the lower atmosphere.

Table 3-16: Radiative transfer input data per sensor.

	GOME-2	OMI	TROPOMI
Snow/ice flag, land/ocean flag	NO ₂ OFL	O ₂ – O ₂ cloud	NO ₂ OFL
Cloud fraction, Cloud pressure	NO ₂ OFL	O ₂ – O ₂ cloud	NO ₂ OFL
Surface pressure / surface altitude	NO ₂ OFL	O ₂ – O ₂ cloud	NO ₂ OFL



A priori profile shapes	MAGRITTE simulations at 9h30 local time	MAGRITTE simulations at 13h30 local time
Surface albedo	Kleipool et al. 2008	

Empirical correction for strong NO₂ absorption

The fitting approach used in Eq. 3-14, which fits a single slant column value for all wavelengths, relies on the assumption that the effective light path through the atmosphere is independent of the wavelength. In the case of strong absorption by one or more species, this assumption may no longer hold, and the quality of the fit is degraded. For glyoxal retrievals in the 435-460 nm fitting window, extreme NO₂ concentrations can have this effect. Pukite et al. (2010) have shown that fitting additional cross sections which represent the Taylor expansion of a wavelength-dependent slant column, can compensate the error, but this comes at the cost of increased scatter in the retrieved SCD's, especially in regimes with low NO₂ SCD's. Therefore, we opt for an empirical correction of the glyoxal SCD, using a linear function of the fitted NO₂ SCD:

$$\Delta \text{SCD}_{\text{CHOCHO}} = -8.75 \cdot 10^{12} \text{ molec. cm}^{-2} - 7.01 \cdot 10^{-3} \text{ SCD}_{\text{NO}_2} \quad \text{Eq. 3-16}$$

where the correction coefficients in Eq. 3-16 have been determined from a sensitivity test comparing fitted glyoxal SCD's with and without the additional Pukite terms in regimes with high NO₂ SCD's (Lerot et al., 2021).

Background correction

Systematic biases in the retrieved SCD's remain, due to interferences with spectral signatures from other absorbers, or due to instrumental effects. In order to reduce these biases, we apply a background correction using observations in a reference sector in the equatorial Pacific, where we assume a homogeneous background glyoxal vertical column density

$$\text{VCD}^{\text{ref}} = 1 \cdot 10^{14} \text{ molec. cm}^{-2} \quad \text{Eq. 3-17}$$

For any satellite observation, this reference VCD can be translated into a corresponding SCD^{ref} using the observation's air mass factor:

$$\text{SCD}^{\text{ref}}(\text{obs}) = \text{VCD}^{\text{ref}} \cdot \text{AMF}(\text{obs}) \quad \text{Eq. 3-18}$$

The background correction consists of correcting for the mean difference between the retrieved slant column SCD(obs) and the corresponding SCD^{ref}(obs) for observations in the reference sector. The following sections describe the exact correction procedure as well as selection criteria for reference spectra for each of the three the instrument types.

GOME-2

Latitude bins	8 bins of width 10°, between 40°S and 40°N
Viewing zenith angle bins	11 bins of width 10°, between -55° and 55°
Longitude limit	180°E – 250°E
Filter criteria	<ul style="list-style-type: none"> • “effective cloud fraction” < 0.2





	<ul style="list-style-type: none"> • No snow/ice scenes • $SZA < 70^\circ$ • $RMS\ residual < 2e-3$ • $RMS\ residual < mean(RMS) + 2*std_dev(RMS)$ • VCD within 3 standard deviations of the mean VCD • $SCD_liquid_water < median(SCD_liquid_water) + std_dev(SCD_liquid_water)$ • No backscan pixels
--	---

For the GOME-2 instruments, we split the observations in the reference sector into latitude and viewing zenith angle (VZA) bins (i, j) , $i = 1 \dots N_{lat}$, $j = 1 \dots N_{VZA}$. In a first step, we compute a VZA-dependent offset: for each VZA bin j , we compute the mean difference of the observed SCD and the reference SCD, for the observations from all latitude bins inside the equatorial range $20^\circ S - 20^\circ N$:

$$\Delta_{VZA}(j) = \frac{1}{N_{obs}} \sum_{obs\ in\ bins\ with\ |lat| < 15, VZA\ bin\ j} (SCD(obs) - SCD^{ref}(obs)) \quad \text{Eq. 3-19}$$

Next, we compute the remaining latitude-dependent offset after subtracting the VZA-dependent offset for the corresponding VZA bin from each SCD. For each latitude bin i , we compute the mean offset over all VZA bins:

$$\Delta_{lat}(i) = \frac{1}{N_{obs}} \sum_{obs\ in\ lat\ bin\ i, all\ VZA\ bins} (SCD(obs) - \Delta_{VZA}(j_{obs}) - SCD^{ref}(obs)) \quad \text{Eq. 3-20}$$

Where j_{obs} is shorthand for “the VZA bin of the current observation”.

We then compute correction factors for every latitude and viewing zenith angle by fitting a continuous function through these discrete offsets. We use a cubic spline interpolation $\Delta_{VZA}(\theta)$ for the VZA-dependent correction, and a linear fit $\Delta_{lat}(l)$ for the latitude-dependent correction, extrapolating for latitudes outside of the reference sector, and correct every SCD as follows:

$$SCD^{BC} = SCD - \Delta_{VZA}(\theta) - \Delta_{lat}(l) \quad \text{Eq. 3-21}$$

where θ and l are the corresponding viewing zenith angle and latitude, respectively.

OMI

Latitude bins	4 bins of width 20° , between $40^\circ S$ and $40^\circ N$
Longitude limit	$180^\circ E - 250^\circ E$
Filter criteria	<ul style="list-style-type: none"> • Cloud fraction < 0.2 • No snow/ice scenes • $SZA < 70^\circ$ • $RMS\ residual < 1.5e-3$





	<ul style="list-style-type: none"> • RMS residual < mean(RMS) + 2*std_dev(RMS) • VCD within 3 standard deviations of the mean VCD • SCD_liquid_water < median(SCD_liquid_water) + std_dev(SCD_liquid_water) • Abs(Radiance_shift) < 0.005nm (to filter pixels affected by the OMI row anomaly)
--	---

For OMI, we split the observations in the reference sector into to latitude and detector row bins $(i, r), i = 1 \dots N_{lat}, r = 1 \dots 60$. The first step consists of computing a row-dependent offset, or destriping correction: for each detector row r , we compute the mean difference of the observed SCD and the reference SCD, for all observations in the latitude bins inside the equatorial range 20°S-20°N:

$$\Delta_{stripe}(r) = \frac{1}{N_{obs}} \sum_{\text{obs in bins with } |lat| < 15, \text{ row } r} (SCD(\text{obs}) - SCD^{ref}(\text{obs})) \quad \text{Eq. 3-22}$$

Next, we compute the remaining latitude-dependent offset after subtracting the stripe correction for the corresponding row from each SCD. For each latitude bin i , we compute the mean offset over all rows:

$$\Delta_{lat}(i) = \frac{1}{N_{obs}} \sum_{\text{obs in lat bin } i, \text{ all rows}} (SCD(\text{obs}) - \Delta_{stripe}(r_{obs}) - SCD^{ref}(\text{obs})) \quad \text{Eq. 3-23}$$

where r_{obs} is shorthand for the detector row of the current observation. Using these offsets per row and latitude bin, we correct each slant column as follows:

$$SCD^{BC} = SCD - \Delta_{stripe}(r) - \overline{\Delta_{lat}} \quad \text{Eq. 3-24}$$

where $\overline{\Delta_{lat}}$ is the average correction over all latitude bands.

TROPOMI

Latitude bins	4 bins of width 20°, between 40°S and 40°N
Longitude limit	165°E – 220°E
Fiter criteria	<ul style="list-style-type: none"> • Cloud fraction < 0.2 • No snow/ice scenes • SZA < 70° • RMS residual < 1.5e-3 • RMS residual < mean(RMS) + 2*std_dev(RMS) • VCD within 3 standard deviations of the mean VCD





For TROPOMI, observations are assigned to latitude and detector row bins as well. In the first step, we calculate a destriping correction $\Delta_{\text{stripe}}(r)$ for each of the 450 TROPOMI detector rows following Eq. 3-19.

The destriping correction helps to remove high frequency row-dependent bias, but a residual broadband row-dependent structure in the slant columns remains. The origin of this row-dependence is not understood, but we add an additional smoothly varying correction to reduce it. To this end, we assign the observations in the reference sector to 20° latitude bins $i = 1 \dots 4$, between 40°S and 40°N, and row bins $j = 1 \dots 30$, each of which contains the observations from 15 adjacent detector rows. We then compute a mean offset per latitude and row bin as follows:

$$C(i, j) = \frac{1}{N_{\text{obs}}} \sum_{\text{obs in bin}(i, j)} \left(\text{SCD}(\text{obs}) - \Delta_{\text{stripe}}(r_{\text{obs}}) - \text{SCD}^{\text{ref}}(\text{obs}) \right) \quad \text{Eq. 3-25}$$

In order to preserve the global latitudinal distribution of the background SCD's, of which we have poor a priori knowledge, and correct only an overall bias, we subtract the mean offset over all row bins for each latitude, and add the overall mean offset the offsets, leading to modified offsets $C'(i, j)$:

$$C'(i, j) = C(i, j) - \frac{1}{30} \sum_k C(i, k) + \frac{1}{120} \sum_k \sum_l C(k, l) \quad \text{Eq. 3-26}$$

We then interpolate these modified offsets $C'(i, j)$ per latitude and row bin using a two-dimensional spline interpolation to obtain correction factors $C'(l, r)$ for all latitudes and rows. Using these offsets, we calculate the corrected slant column as follows:

$$\text{SCD}^{\text{BC}} = \text{SCD} - \Delta_{\text{stripe}}(r) - C'(l, r) . \quad \text{Eq. 3-27}$$

3.4.3. Information content and uncertainty estimate

Many factors contribute to the retrieved glyoxal tropospheric column uncertainty: detector noise as well as systematic errors affecting fitted the slant columns, uncertainties on a priori information such as profile shapes and the reference sector background concentration, errors in auxiliary data such as surface albedo, or radiative transfer modelling errors. Table 3-17 provides an overview of the different contributions and their typical order of magnitude. We refer to the End-to-End ECV Uncertainty Budget document for a detailed analysis of the uncertainties affecting glyoxal retrievals.

Table 3-17: Glyoxal tropospheric vertical column density retrieval uncertainty components

Error source	Order of magnitude [molec. cm ⁻²]
Slant column retrieval random error	$6 \times 10^{14} - 1 \times 10^{15}$ (TROPOMI)
Slant column retrieval systematic uncertainty	$5 \times 10^{13} - 1 \times 10^{14}$
Air mass factor uncertainty	$1 \times 10^{13} - 1 \times 10^{14}$
Background correction uncertainty	$5 \times 10^{13} - 1 \times 10^{14}$
Total systematic uncertainty	$1 \times 10^{14} - 3 \times 10^{14}$







3.5. Carbon monoxide (L2-CO)

3.5.1. Overview

Our objective is to generate a homogenized and merged CO L3 CDR dataset.

For that, we will use satellite data from two instruments as input: IASI and MOPITT. The IASI CO L2 data consist in a reprocessed dataset, performed by EUMETSAT in 2021.

In cycle one of WP 304, we produced an intermediate product: we post-processed IASI CO L2 data (in two steps: outliers filtering + reformatting and then cloud filtering) and averaged Metop-A, B and C data in order to get a new IASI CO L3 product: multi-platform monthly grids (L3). At the time of writing this document, this new intermediate dataset has been sent to BIRA for validation.

In cycle two of WP 304, we will work on merging this new IASI dataset and MOPITT V9T data (using corrective factors) in order to built a homogenized and merged CO L3 CDR dataset.

We summarized the different steps in Figure 3-7.

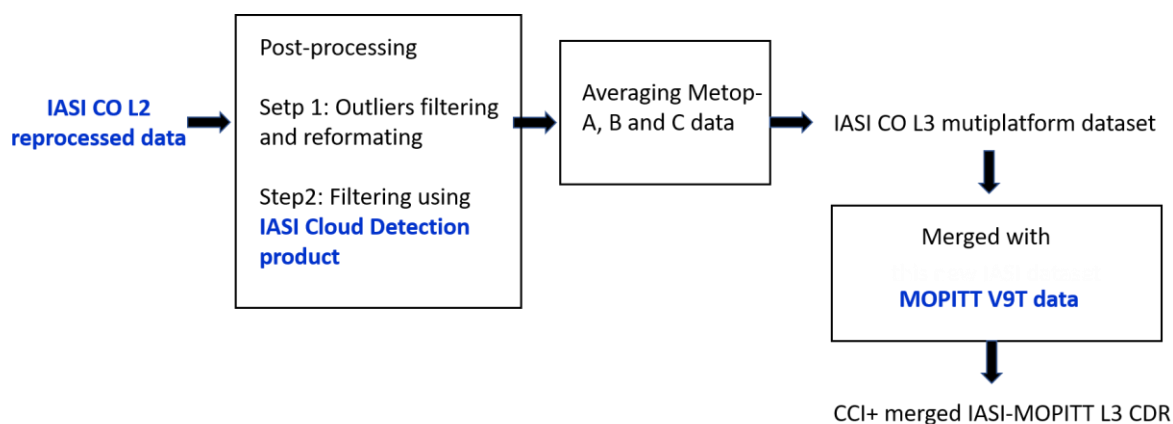


Figure 3-7: Graphic representation of the processing steps. Satellite input data are in blue.

In this section we will describe the different input satellite data and their corresponding algorithms. The description of L3 production will be given in section 3.5.

3.5.2. Algorithm description

IASI and MOPITT CO L2 products

In this work, we use the IASI L2 CO reprocessed data from EUMETSAT, called Climate Data Record (CDR) for Metop A and Metop B. In fact, EUMETSAT reprocessed the whole IASI CO data record between 2020 and 2021 and the CO CDR are available until December 2021. This was done to process the L1C IASI data with the most recent version of the auxiliary IASI data used as input (temperature, humidity and cloud information; all EUMETSAT products) with

the latest FORLI version. The whole time series of IASI-CO, for the first time, has been made homogeneous. Metop C data (2019 onwards) is running with the latest algorithm.

Note that the EUMETSAT IASI L2 CO reprocessed are called IASI CO Climate Data Record (CDR). It should not get mixed up with CCI CO CDR which is the final product that will be produced within the project, that is a homogeneous and merged IASI-MOPITT L3 product.

IASI CO L2 data have been retrieved using the Fast Optimal/Operational Retrieval on Layers for IASI (FORLI), a dedicated radiative transfer and retrieval software for IASI. It was developed at the Université Libre de Bruxelles (ULB; Hurtmans et al., 2012) in collaboration with LATMOS/IPSL, with the objective to provide global concentration distributions of atmospheric trace gases. For the inversion step, it relies on a scheme based on the widely used Optimal Estimation theory (Rodgers, 2000). The software has been set-up to process IASI level 1C radiances for vertical profile retrievals of CO and has been implemented at EUMETSAT. The FORLI CO Algorithm Theoretical Basis Document is available online (Astoreca et al., 2014).

IASI L2 CO product has been extensively validated. In the framework of the AC SAF project, Validation Report of the reprocessed IASI L2 CO CDR has been reviewed and will be available online in the coming months.

MOPITT v9T data

MOPITT (Measurements of Pollution in the Troposphere) is a gas correlation radiometer instrument on the NASA Terra satellite which permits retrievals of CO vertical profiles using both thermal-infrared (TIR) and near-infrared (NIR) measurements. MOPITT instrument has been in operation since 2000 (Drummond et al., 2016), resulting in a long-term data record. CO retrievals are obtained by using a maximum a posteriori method that incorporates a priori information of the physical and statistical variability of the trace gas distribution in the atmosphere. For this study we use MOPITT V9T data. The MOPITT CO Algorithm Theoretical Basis Document is available on line (Francis et al., 2017). MOPITT L2 CO data have been extensively validated (Deeter et al., 2022).

IASI Cloud Detection Product

The “IASI Cloud Detection” product is a new cloud mask available at the IASI pixel level (L2) that was developed by Simon Whitburn at ULB, for climate applications purposes. It is a different product from the EUMETSAT Cloud product used when retrieving IASI CO L2 with FORLI. It combines a high sensitivity to cloud detection, a very good consistency over time and between the three IASI instruments and simplicity in its parametrization. The method is based on the use of a supervised neural network using the version 6.5 of the operational IASI L2 cloud product as a reference dataset. As input parameters, it relies on IASI radiance information only. The consistency over time is ensured by careful selection of the IASI input channels, avoiding especially the spectral regions affected by long-lived absorbers and water vapor. The IASI Cloud Detection algorithm’s description and validation are presented in Whitburn et al. (2022). In the project, this independent improved cloud product will be used



a posteriori on the IASI CO data (already filtered with a EUMETSAT cloud product), in order to get a “cleaner” product if possible.

3.5.3. Uncertainty estimate

For this section, we refer to the E3UB document where an analyse of the CO uncertainty on global and local scale is presented. On global scale, mean uncertainty for daytime measurements is $1.4 \cdot 10^{17}$ molecules/cm² with a standard deviation of $0.1 \cdot 10^{17}$ molecules/cm² for both Metop-A and Metop-B. For nighttime, the mean uncertainty is larger: $1.7 \cdot 10^{17}$ molecules/cm² [std: $0.1 \cdot 10^{17}$ molecules/cm²]. Uncertainty time series for the whole globe is shown in Figure 3-8.

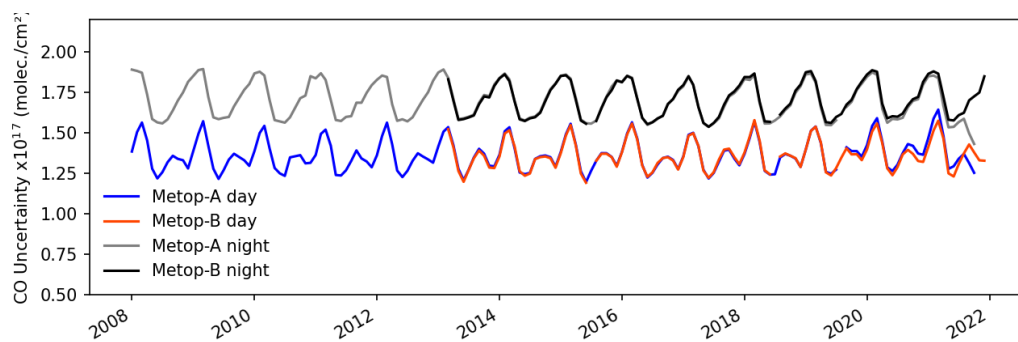


Figure 3-8: CO uncertainty time series for the globe, for day time and night time measurements, for both Metop-A and Metop-B.

3.6. Ammonia (L2-NH₃)

This section describes the ANNI v4 NH₃ retrieval algorithm (level 2) for IASI onboard Metop-A, B, and C, developed at the ULB. The retrieval algorithm is part of a chain of retrieval algorithms called the ANNI (Artificial Neural Network for Infrared Atmospheric Sounding Interferometer, IASI) retrieval framework, for the retrieval of short and medium long-lived trace gases, see Franco et al. (2018). The historical development, theoretical basis and background has been documented in a series of papers: Whitburn et al. (2016), Van Damme et al. (2017), Franco et al. (2018), Van Damme et al. (2021) and Clarisse et al. (2023). Most of the text and some figures below are taken from these publications. Some material is also taken from Clarisse et al. (2019), and some is original.

3.6.1. Retrieval overview

A schematic overview of the ANNI retrieval is presented in **Error! Reference source not found.** Figure 3-9. The actual calculation of the columns (red boxes in Figure 3-9) relies on two computational steps:

1. The calculation for each IASI observation of a hyperspectral range index (HRI). This quantity is a very sensitive, broadband spectral index that quantifies the signal strength of a target absorber in a radiance spectrum.
2. The conversion of the HRI into a total column abundance via an artificial feedforward neural network (NN).

In addition to the HRI, the NN relies on a series of auxiliary parameters related to the state of the atmosphere and of the surface. Perturbations to the input data of the NN allows quantification of the uncertainties associated with single pixel retrieved columns. The neural network is also employed for the calculation of total column averaging kernels. Appropriate filtering of the data (before and after the retrieval) removes cloudy scenes and observations with limited or no sensitivity to the target trace gas. Finally, in general (for most species in the ANNI retrieval framework), a calibration offset is added to the retrieved columns to account for the constant, climatological background column of the target gas in the atmosphere (green box in Figure 1). However, this last step is not done for NH₃, as background concentrations are extremely low and below the detection limit of IASI.

While the retrieval itself is simple and fast, the initial setup (blue and red boxes in Figure 3-9) of the HRI and NN is nontrivial. In particular, both rely on weight constants that must be determined with care beforehand from a data set of real (for the HRI) and synthetic (for the NN) IASI spectra. The setup of the HRI and NN and the training of these weight constants are detailed in sections 3.6.2 and 3.6.3. The calculation of the AVKs is detailed in section 3.6.4.

Running the NN relies on a series of (meteorological) input data that is different for each observation. The ANNI v4 NH₃ product exists in two flavours, depending on the origin of this input data. Whereas the baseline product (also called near-real time (NRT) product) uses operational IASI Level 2 (L2) information on the pressure, humidity and temperature profiles and a climatology characterizing the boundary layer height, the reanalysed product uses ERA5



model output for these parameters (Hersbach et al., 2020), interpolated in time and space to match the observations. The resulting product is temporally more consistent as it removes the effect of the several changes that occurred in the L2 products throughout the years. Both NH_3 products include several empirical corrections to counter small differences observed between the three IASI instruments and small biases that occurred because of sporadic changes to the IASI instrument or in the L0 to L1c processing of the spectra. The actual retrieval is presented in section 3.6.5., which also includes information on pre and post filtering flags, and uncertainty calculation. Examples are presented in 3.6.6. Section 3.6.7 summarizes the main advantages of the retrieval algorithm. Finally, we present a comparison of the ANNI retrieval with an OEM retrieval.

Artificial Neural Network for IASI (ANNI) framework

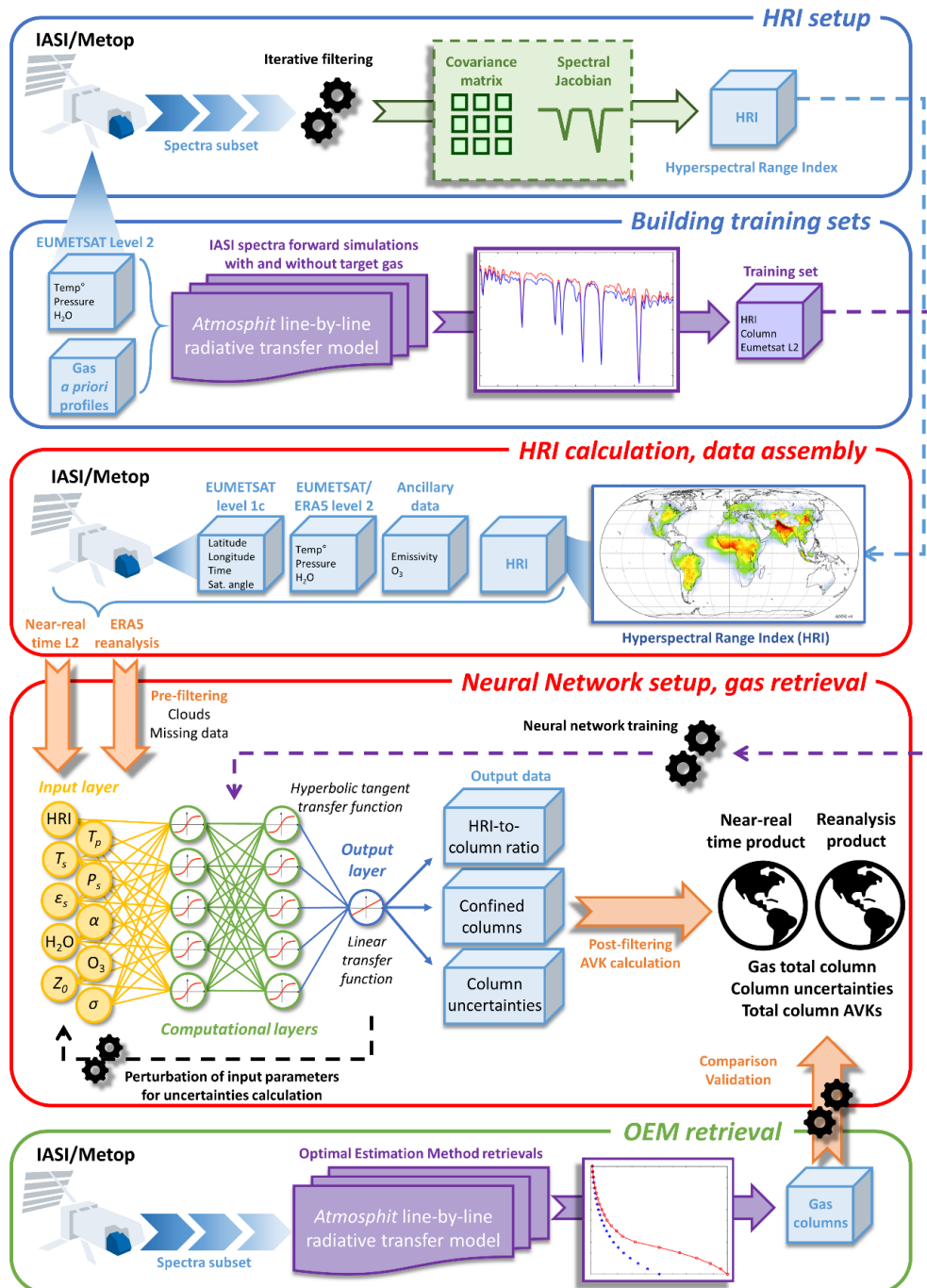


Figure 3-9: Conceptual flowchart of the ANNI retrieval method for NH₃.

3.6.2. HRI

Definition



Proposed by Walker et al. (2011), the HRI is a dimensionless index that quantifies the strength of the spectral signature of a target gas in an observed spectrum y :

$$\text{HRI} = \frac{K^T S_y^{-1} (y - \bar{y})}{\sqrt{K^T S_y^{-1} K}} \frac{1}{N}$$

where K is a spectral Jacobian, S_y a covariance matrix, and \bar{y} the mean spectrum generated from a representative data set of background spectra associated with a climatological column of the target gas, and N an extra normalization factor (see further). The HRI is conveniently normalized to have a mean of zero and a standard deviation of one when calculated on the data set of background spectra. The HRI is particularly suitable for the detection of highly variable infrared absorbers, like NH_3 , which are not observed in every spectrum. In this case, the climatological column amount is close to zero and the background spectra are those without observable signature of NH_3 . The HRI can encompass spectral ranges of up to several hundred cm^{-1} to exploit all the channels in which the target species is absorbing. This results in a substantial gain of sensitivity over other detection methods and makes it highly suitable for the detection of broadband absorption features, as demonstrated with the detection of a series of aerosol types in Clarisse et al. (2013).

Spectral range and Jacobian

Larger spectral ranges lead in principle to a more sensitive HRI. However, this is true only in the linear regime in which the covariance matrix describes a normal distribution. In practice, it can be advantageous to exclude spectral ranges where nonlinearity prevails. For instance, the spectral range 1,100–1,200 cm^{-1} can exhibit pronounced spectral surface emissivity features over deserts. In addition, it might be useful to avoid a spectral interval in which another species with a similar spectral signature is absorbing. For NH_3 the range was set to 812–1,126 cm^{-1} that exploits the strongest lines from its ν_2 vibrational band. A wider spectral range was chosen to minimize interferences with surface emissivity features. The Jacobian K is the derivative of the radiance spectrum with respect to the column abundance of the target species, and this was generated by the line-by-line radiative transfer model Atmosphit (Coheur et al., 2005) for a standard atmosphere.

Characterization of mean and covariance

For each target species, the HRI calculation also depends on a generalized covariance matrix S_y and an associated background spectrum \bar{y} . The covariance matrix determines the weight of each spectral channel, and ideally expresses the variability and covariance of all interfering species, but explicitly not that of the target species (Walker et al., 2011). Such a matrix can be obtained from a representative set of IASI spectra with a constant, climatological column amount of the target species. For short-lived trace gas absorbers like NH_3 , the pair (S_y, \bar{y}) can straightforwardly be constructed from spectra with no observable signature of the gas (the associated climatological column is then close to zero). To select such spectra, an iterative approach can be followed (Clarisse et al., 2013). The approach goes like this. First, a representative set of IASI spectra is built, consisting of all the spectra from the fifteenth of





each month of 2013 but sampled to yield a spatially uniform distribution (to avoid over-representing polar regions). This entire set is then used for the generation of a first (S_y, \bar{y}) pair. This allowed the production of a first set of HRI, which in turn was used to remove the spectra with detectable signatures of the trace gas (typically with an HRI above 3 or 4; see below). The reduced set of spectra allows the calculation of a better (S_y, \bar{y}) pair. Repeating this process several times (typically at least 10 times) leads to convergence of the set of spectra, of the corresponding (S_y, \bar{y}) , and of the HRI.

An even more sensitive HRI could be constructed by considering only the spectra with an HRI below one. Using such a low threshold removes much more spectra, including those with spectral signatures barely above the instrumental noise and even spectra without detectable gas quantities. This is obvious for NH_3 , where spectra above remote oceans frequently exhibit HRIs below one. Nevertheless, removing such spectra leads to a more sensitive HRI and does not generate anomalies (e.g., false detections). There is, however, a side effect, in that the initial normalization of the HRI is not preserved in the iterative process. This is the reason why an additional normalization factor (N) is needed in the calculation of the HRI. Note that this factor N needs to be recalculated at each iteration. The normalization factor N was calculated as the standard deviation of the HRI over a remote ocean area, where no NH_3 is expected.

In total 24 iterations were carried out for the construction of the covariance matrix. In addition to all observations with an HRI below one, also observations over selected desert regions were included at each iteration, these include most notably, the Saharan Desert, Arabian desert, and parts of the Great Simpson, as no NH_3 is expected for those, and to make the HRI more robust for the emissivity features found over deserts.

Pseudoinverse

The generalized error covariance matrix S_y plays a key role in the calculation of the HRI. As a symmetric matrix, S_y has real eigenvalues λ_i and can be decomposed as

$$S_y = \sum_{i=1}^n \lambda_i \vec{s}_i \vec{s}_i^T$$

with all \vec{s}_i orthogonal to each other. It follows that its inverse can be written as

$$S_y^{-1} = \sum_{i=1}^n \frac{1}{\lambda_i} \vec{s}_i \vec{s}_i^T$$

The distribution of the eigenvalues of the covariance matrix used for the NH_3 HRI (with a spectral range covering 812 to 1126 cm^{-1}) is shown in **Error! Reference source not found.** Three domains can be distinguished: (i) the 30 highest values, corresponding to the principal components, (ii) around 1200 values corresponding mainly to instrumental noise and (iii) around 20 very small eigenvalues. These smallest eigenvalues are of the order of the numerical precision at which the covariance matrix is calculated, and in essence correspond to directions not occurring in IASI spectra. While random instrumental noise would be expected to occur in all directions, apodization and L1 post-processing remove some. Such





directions carry the most weight in S_y^{-1} but as they are not found in real spectra they do not contribute much to the total HRI (as can easily be verified numerically).

However, small changes to the instrument calibration or post-processing can alter the contribution of these directions in the IASI spectra, and because they carry such a large weight in the HRI, they can affect its value considerably. This explains why the HRI in the past has been found to be very sensitive to such changes. It also explains the occurrence of (small) biases between the different instruments. The solution is fortunately simple (Rodgers et al., 2003; Eaton, 2007), and is obtained by disregarding the terms corresponding to the very small eigenvalues. As we will show in the next section, using such a pseudoinverse does not eliminate the effects of L1C changes completely, but reduces their magnitude considerably.

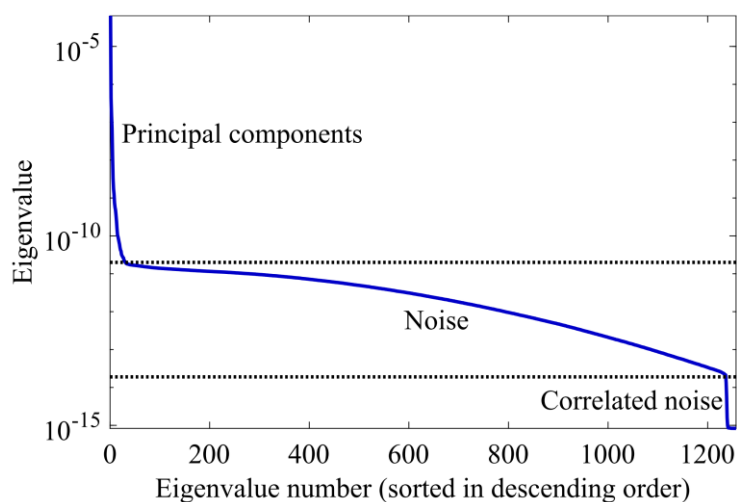


Figure 3-10: Eigenvalue spectrum of the covariance matrix S_y used for the calculation of the HRI of NH_3 . The eigenvalues are ordered from largest to smallest.

Detrending and anomaly corrections

As the mean spectrum and covariance matrix that are used for the HRI are calculated from spectra measured within one reference year (2013), long-term changes in atmospheric composition that affect the spectral region of interest, can have unwanted effects on the HRI. This was first noted in Van Damme et al. (2021), where a spurious trend was seen in the HRI NH_3 data over remote regions. It was attributed to the increase in global carbon dioxide (CO_2) concentrations, because of the presence of a weak CO_2 absorption band in the 920-990 cm^{-1} spectral region (Whitburn et al., 2021) where NH_3 has its strongest absorption. A linear correction on the HRI of the order of 0.03 per year was introduced to compensate for this effect. However, because of seasonal variations, and possible temperature dependence of the interference, an HRI which is less sensitive to CO_2 changes is preferable. One option is to build the covariance matrix from spectra spanning the entire period of IASI measurements.

An alternative approach is to account directly for the effects of CO_2 in the calculation of the HRI. The HRI formula is related to generalized least squares estimation and can be expanded



to include multiple variables that are simultaneously estimated (Walker et al., 2011; Theys et al., 2022). In our case, the Jacobian vector becomes a two-column matrix, one column corresponding to NH_3 and the other to CO_2 . The HRI formula remains formally identical (with only the first component of the two-element HRI vector of interest).

The stability of the HRI was evaluated over ten remote regions, where only background columns of NH_3 are expected. Their average monthly HRI is shown in **Error! Reference source not found.** for the three IASI instruments separately. The top panel shows the average as obtained with the HRI setup as described above, i.e., with pseudoinverse and with a CO_2 Jacobian. As with previous versions of the product, a spurious linear trend is observed, but thanks to the introduction of the CO_2 Jacobian, its magnitude is reduced to about 0.01 per year, compared to 0.03 per year previously. A slightly steeper decrease is observed for Metop B. We correct for these trends by adding a time-dependent offset as in Van Damme et al. (2021). The result after correction is shown in the second panel of **Error! Reference source not found.**

A detailed analysis was made of this time series to detect offsets between the different instruments and shifts that coincide with known changes in the IASI L1C data. The largest of these is the offset of 0.11 seen between IASI-C and the two other instruments. Small offsets in the HRI time series of IASI-A were found in 2010, 2015 and 2017 and in the HRI of IASI-B in 2015. For each of these, offset corrections were calculated in the range of 0.01-0.03. Thanks to the pseudoinverse, their magnitude is drastically reduced (previously, offsets as large as 0.6 were observed). The resulting corrected time series is shown in the third panel. This time series is temporally stable and shows an excellent consistency between the three instruments, but exhibits a weak seasonal cycle, likely due to the combined effect of seasonal changes in the concentrations of H_2O and volatile organic compounds that absorb in the same spectral range as NH_3 . To remove this seasonality an offset depending on latitude and month of the year was calculated from 2012-2014 IASI-A data and applied on all data. The HRI after correction is shown in the bottom panel of **Error! Reference source not found.** Thanks to the improved setup of the HRI, and the new cloud product, the magnitude and therefore also uncertainty of all these corrections is lower than in the previous product, which in the end results in much improved temporal consistency.

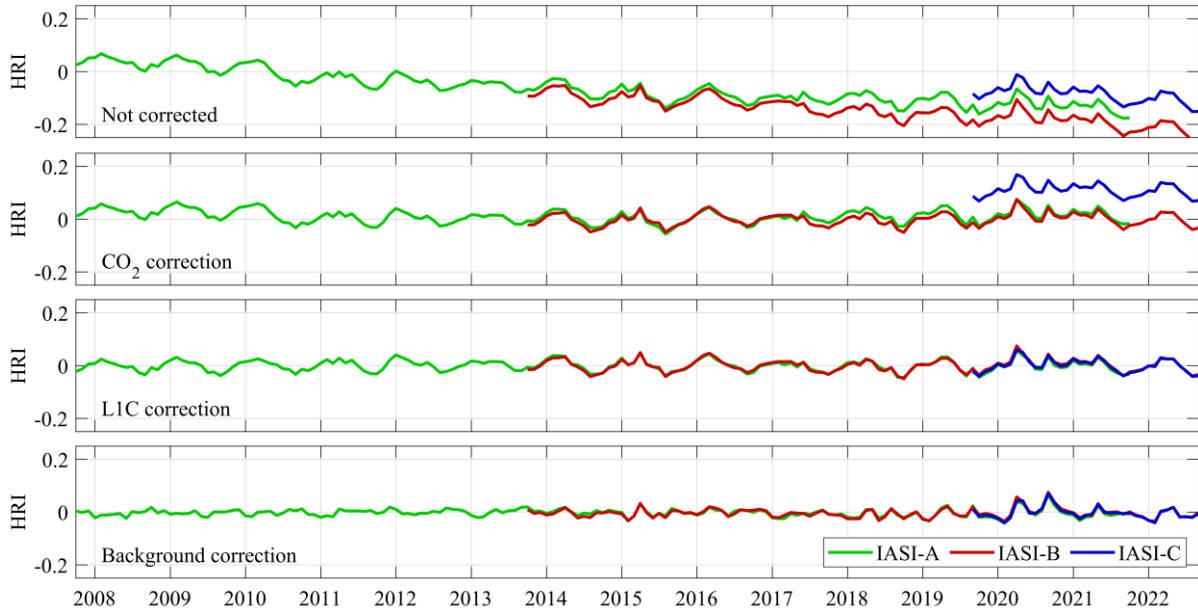


Figure 3-11: Monthly average HRI time series over 10 remote regions for the three IASI instruments separately. The top panel shows the uncorrected timeseries, and the other panels, from top to bottom, show the effects of the corrections that are applied consecutively.

3.6.3. The neural network

The spectral signature (the HRI) of a target gas is a complex function of the species abundance and of all the other parameters entering the radiative transfer, such as the state of the atmosphere (thermodynamic parameters) and surface, interfering species, and the viewing angle. The main idea of the ANNI retrieval approach is to use a neural network (NN) to approximate the complex inverse function that maps the HRI and the auxiliary parameters to a column abundance. In particular, the measured HRIs are related to estimates \hat{X}^a of the true NH_3 total columns X , via a scaling factor SF^a

$$\hat{X}^a = \frac{\text{HRI}}{SF^a}$$

In the retrieval, a specific vertical profile is assumed for NH_3 , but otherwise the retrieval is entirely unconstrained. The superscript “a” refers to this vertical profile assumption. In particular, we assume that the total column \hat{X}^a is vertically distributed according to an a priori vertical partial column profile:

$$a_z = \frac{\hat{X}_z^a}{\hat{X}^a}$$

with $\sum_z a_z = 1$.

Training set assembly

The scaling factors that are thus calculated in the ANNI retrieval framework with a NN. A NN consists of interconnected nodes (small mathematical functions) organized in layers, as





illustrated in **Error! Reference source not found.** (lower red box). The weights of the nodes are trained to best fit the complex analytical relationships that bind any set of input variables feeding the network, to the corresponding output variable. NNs learn from the presentation of examples, and so training sets are required consisting of matching input (auxiliary parameters, column abundance) and output data (IASI spectrum and associated HRI).

The performance of a NN depends largely on the quality of the training set, which should be as comprehensive and representative as possible. This means that in our case, the set should cover a large range not only of the column abundances of the target trace gas (and associated HRI) but also of the auxiliary parameters on the state of the atmosphere and surface. Each IASI observation (L1C radiance spectra) is distributed operationally with corresponding Level 2 data consisting of a temperature, pressure, H₂O profile, and surface temperature (August et al., 2012). These were used here as input for the auxiliary parameters of the training data set. We selected approximately 500,000 IASI L2 data over the year 2013, regularly sampled in space and time to ensure a comprehensive and representative data set.

As the surface temperature and emissivity vary more over land than over oceans, 66 % of the data were chosen to be associated with land observations. Additional data were added for the higher and lower thermal contrasts TCs (defined as the temperature difference between the surface and the air layer located just above) to ensure that extreme TCs are sufficiently represented within the training data set. Finally, a random column of the target trace gas was associated with each sample in the data set. These random columns were generated by randomly scaling a vertical profile of the gas for a wide range of total columns (**Error! Reference source not found.**, left). Figure 3-13 illustrates the spatial distribution of the resulting data set as well as the sampling as a function of thermal contrast and total column. IASI spectra were simulated for each sample in this data set using Atmosphit. Due to small remaining forward model errors, it was found that HRI values produced by Atmosphit can be biased. For this reason, a spectrum was simulated for each sample with and without the target trace gas. The HRI of the simulation without the target gas was then used to offset the HRI of the other simulation, in such a way that an HRI value of zero always corresponds to the absence of the trace gas. Note that since Atmosphit does not simulate the clouds, the resulting training data set is cloud-free.

As discussed in Whitburn et al. (2016), the vertical profile of NH₃ is parameterized with a Gaussian function as

$$\text{VMR}(z) = \text{VMR}(z_0) e^{-\frac{(z-z_0)^2}{2\sigma^2}}$$

with z the altitude about ground level, z_0 the peak altitude and σ the width of the profile. This parametrization was found to be sufficiently flexible to characterize the vast majority of GEOS-Chem simulated NH₃ profiles (see Figure 3-14). The NN was trained with peak altitudes ranging from 0 to 20 km and σ from 100 m to 3 km (**Error! Reference source not found.**, right). In this way, the NN is fully flexible, and the retrieval is not limited to a specific vertical profile but can be changed according to the needs of the user. Note that a larger number of scenes were



generated with a value of 100 m, as these are used for the generation of averaging kernels (see section 3.6.4).

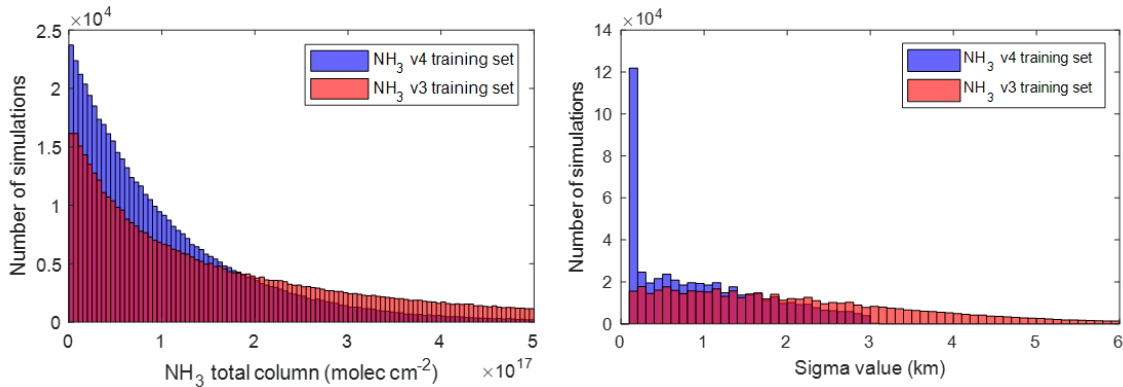


Figure 3-12: Frequency distribution of NH₃ total columns (left) and σ (right) values in the v3 and v4 training set.

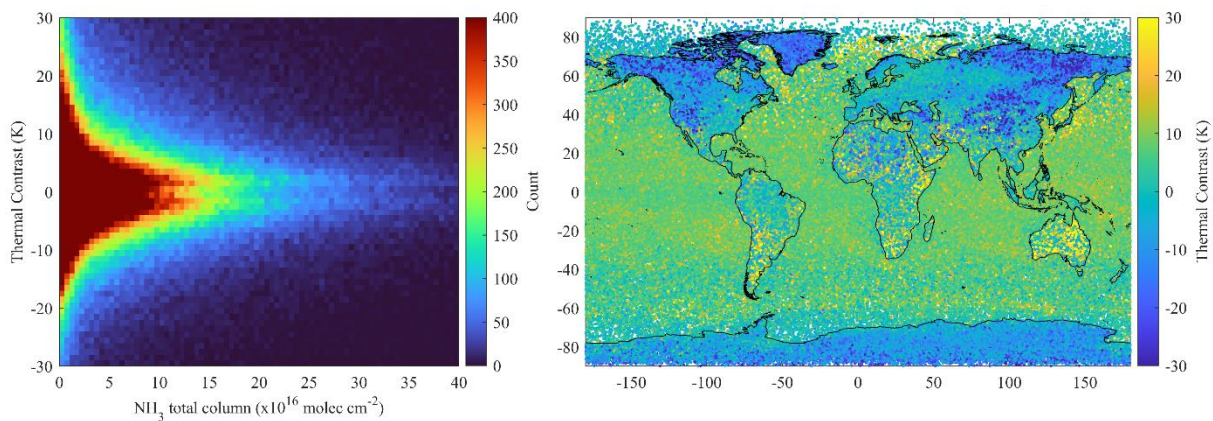


Figure 3-13: Summary statistics on the training set: distribution of thermal contrast vs NH₃ total columns (left), and spatial distribution vs thermal contrast (right).

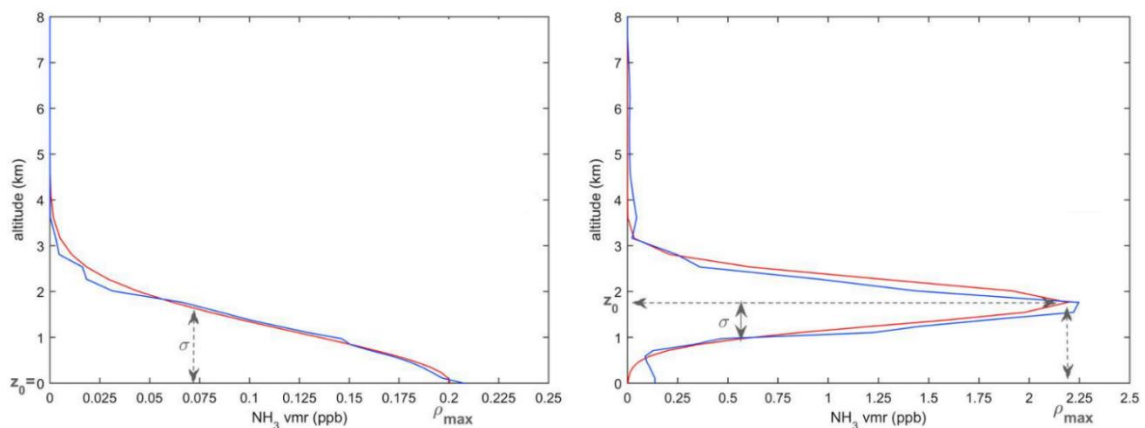


Figure 3-14: Example of GEOS-Chem model (blue) and fitted (red) profiles (left) above a source area and (right) for transported NH₃.





Network setup, training and evaluation

In theory, the input parameters could consist of all the variables used for the forward simulation of the spectra. However, this would result in a very large and difficult data set to train NNs. Instead, it is advantageous to keep the size of the NN as small as possible by only taking into account the parameters that affect most the output variable. A satisfactory network performance was achieved by training with the following input parameters:

- HRI
- temperature profile (T_{prof}) at 0, 0.5, 1, 1.5, 2, 2.5, 3, 5, 7, 10, 13, 16, 19, 25 and 30 km
- skin temperature (T_{skin})
- surface pressure (P_{surf})
- surface emissivity (ϵ_{surf}): average over selected channels in the atmospheric windows
- H₂O partial column profile (H_2O_{prof}) between 0-1, 1-2, 2-3, 3-5, 5-7, 7-10 and 10-30 km
- satellite viewing angle (Z)
- peak NH₃ altitude (z_0)
- Spread of the NH₃ profile (σ)

The HRI-to-column ratio was adopted as output of the NN instead of the gas column itself. The rationale behind this is explained in detail in Van Damme et al. (2017) and Whitburn et al. (2016). In brief, using the ratio allows (1) for a better training of the NN owing to its smaller dynamic scale and (2) to translate the instrumental noise—which is part of the HRI—in a linear way to the retrieved column. In particular, this guarantees that the retrieval on noisy HRI does not lead to a biased product.

Based on the training performances, a NN that consists of two computational layers was setup with each 12 nodes. A multilayer NN is usually better at tackling nonlinearities than a many-node, single-layer network. We have evaluated and improved the setup of the different NNs using 2-D error plots. These summarize the performance of the NN on the training set in terms of relative error and biases as a function of gas total column and thermal contrast. The performance plots are presented in Figure 3-15. Note that normally distributed noise was added to all the input data to evaluate the performances as realistically as possible. The final NNs are seen to be practically unbiased for positive TC. For the non-background gas abundance, the relative errors range from 10% to 50%, with the highest errors found for the low gas columns. The relative errors increase for lower background columns (top panel in Figure 3-15) where the columns approach the IASI detection threshold. However, since the biases remain low (bottom panel), most of these errors can be averaged out by considering multiple observations (thus by averaging the retrieved columns in time or space). In addition, as can be expected, the NNs do not perform optimal for observational scenes with low negative TC.

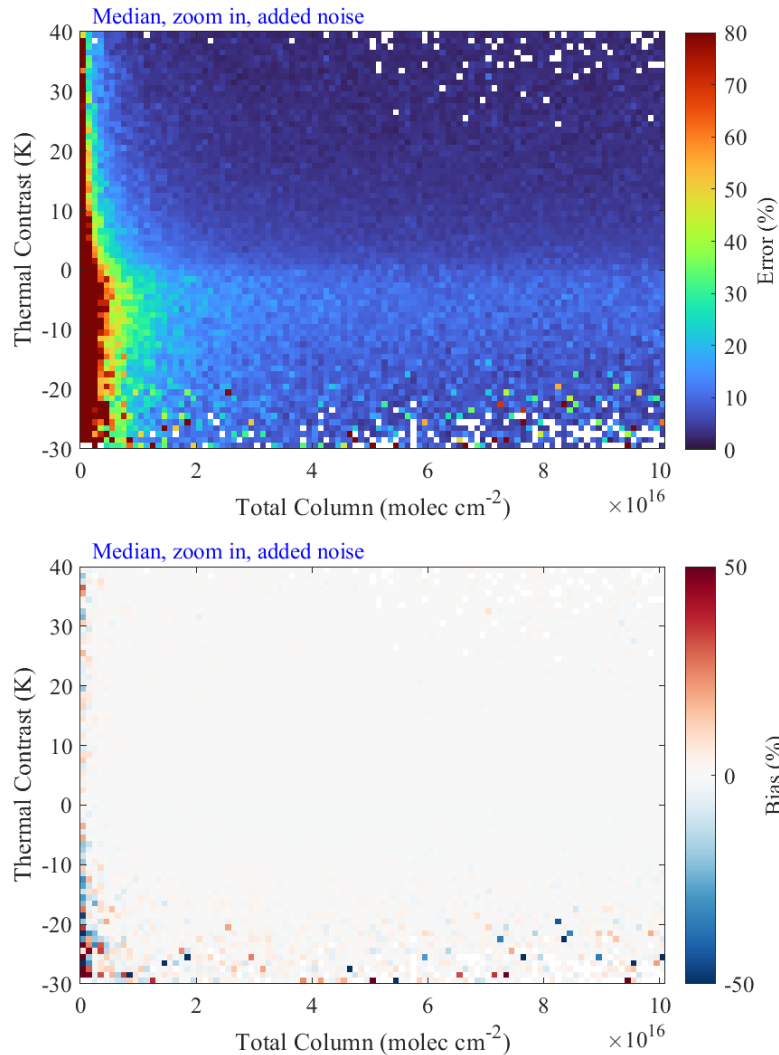


Figure 3-15: Performance evaluation of the neural network, with added noise. The median value is shown in each grid box, which removes the effect of outliers to better reflect the real performance of the network.

3.6.4. Averaging kernels

Linearity and additivity of the HRI

The main assumption on which the AVK formalism, which was introduced in ANNI v4, is based, is that the HRI is approximately linear (proportional to column) and additive, i.e., can be split up in different layer HRIs as $HRI = \sum_z HRI_z$, each linked with a scaling factor SF_z to the partial columns X_z :

$$HRI_z = SF_z X_z$$

We refer to Clarisse et al. (2023) for a discussion on linearity and additivity of the HRI, and why it is valid in the optical thin limit. A graphical demonstration is provided in Figure 3-16.





For the AVK calculation the SF_z are required, and we calculated these by exploiting the flexibility of the NN. Namely, we can calculate the scaling factor $SF^{|z}$ corresponding to the scenario where all NH_3 is presumed to be located in a narrow layer around z using the input parameters $z_{peak} = z$ and $\sigma = 100 m$ for the Gaussian profile. For this calculation, an HRI input parameter is also required, and the choice was made to use the observed HRI. Note that the corresponding column satisfies:

$$\hat{X}^{|z} = \frac{HRI}{SF^{|z}}$$

The scaling factor $SF^{|z}$ is used a good approximation for SF_z .

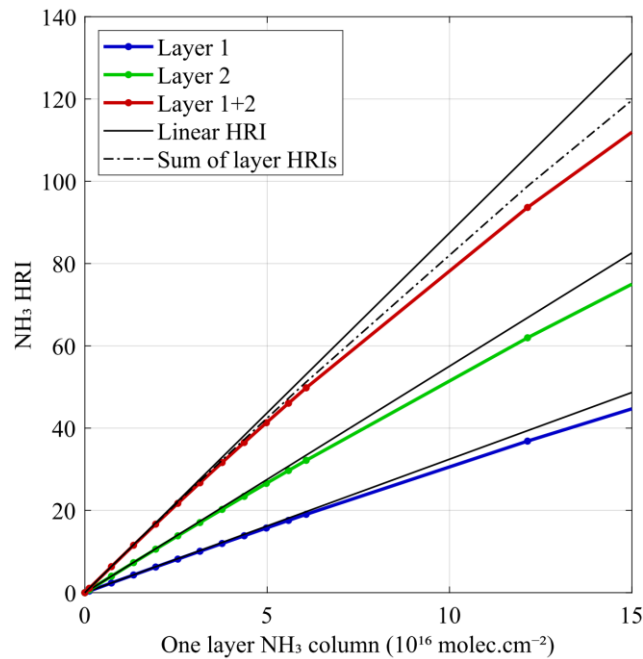


Figure 3-16: Numerical demonstration of the linearity and additivity of the HRI as a function of a change in partial column. In the blue and green scenario, NH_3 was varied at one fixed altitude. In the red scenario, partial columns in both layers were varied simultaneously. The black solid lines represent linearity, whereas the dash dotted line, being the sum of the green and blue curve, represents additivity.

Averaging kernel calculation

The averaging kernel is the matrix A which maps X_z to \hat{X}^a

$$\hat{X}^a = \sum_z A_z^a X_z$$

and can be shown to be equal to (Clarisse et al., 2023)





$$A_z^a = \frac{SF_z}{SF^a} \approx \frac{\hat{X}^a}{\hat{X}^{|z}}$$

with as before $\hat{X}^{|z}$ a column retrieval assuming that the entire column enhancement is confined to layer z . This way of defining the AVK is setup is fully self-consistent, when

$$SF^a = \sum_z SF_z a_z$$

However, to account for slight non-linearities the NN the SF^a are calculated directly, and not through the different SF_z . Consequently, the above equation is only approximately valid, and the factor $N = \sum_z A_z^a a_z$ is not exactly one. A fully consistent AVK can be calculated as:

$$A_z^a = \frac{1}{N} \frac{\hat{X}^a}{\hat{X}^{|z}}$$

And this is how the AVK is calculated in practice. The normalization factor also guarantees that applying the averaging kernels on the a priori vertical profile returns the retrieved column.

3.6.5. Retrieval, uncertainty, and post-filtering

Retrieval overview

The retrieval proceeds in six steps:

1. Observations are pre filtered based on valid L0, L1C and L2 availability, and a cloud flag (Section 3.6.5.2)
2. HRI is calculated and corrected where needed (Section 3.6.2).
3. Other input data to the neural network is gathered (Section 3.6.5.3)
4. Single-pixel uncertainties are calculated (Section 3.6.5.4)
5. Averaging kernels are calculated (Section 3.6.4)
6. Post-filter flags are calculated (Section 3.6.5.5)

We now detail these elements.

Pre-filtering and cloud flags

The pre-filter removes observations with invalid L1C or missing geolocation data. Scenes with a cloud fraction above 25% are also not further processed. For the near-real time product, the cloud fraction originates from the IASI L2. For the reanalysis product the cloud fraction originates from the NN-based cloud product is presented in detail in Whitburn et al. (2022). Trained with data from the latest version (v6.5) of the official L2 cloud product, it inherits all its advantages as a proven and well-validated product. The NN utilises carefully selected IASI channels as input (excluding channels affected by long-lived tracers CO₂, N₂O, CH₄, CFC-11 and CFC-12) and was shown to be temporally consistent, and coherent across the three IASI instruments. The network presented in Whitburn et al. (2022) was trained to distinguish completely clear scenes (0% cloud cover) from the rest. For the NH₃ processing, two additional networks were trained to distinguish scenes with a cloud cover below 10% and 25%





respectively. With this, three cloud flags are available and these are integrated in the v4 of the reanalysed ANNI-NH₃ product.

Retrieval input data

The actual retrieval consists first of collecting the required input data, that is, the HRI of the observed spectrum and the matching auxiliary data. Most of the auxiliary data is directly taken from the IASI L2 or from ERA5, depending on the version of the product (near-real time or reanalysis). Exceptions are the surface emissivity, which originates from Zhou et al. (2013), the HRI which is calculated from the IASI L1C data and the viewing angle, which is also part of the IASI L1C. For ERA5, all parameters are obtained via interpolation of the model's spatial and temporal grid to the exact IASI coordinates (latitude, longitude, and time). One exception is the surface temperature, which is spatially and temporally too variable for model output to be representative for an IASI footprint at a given time. Like the cloud product, a separate NN was trained for the retrieval of surface temperatures, based on the latest IASI L2. Using the output of this network ensures a temporal consistent surface temperature product. As for the NH₃ vertical profile, over ocean, the peak altitude is set to 1.4 km with a σ of 0.9 km (see Whitburn et al., 2016 for a justification). Over land, the peak altitude is set at the surface, with a width σ equal to the boundary layer height. For the near real time product, the boundary layer height is either taken from a monthly day/night climatology (but with the minimum capped at 100 meters, see Figure 3-17). The latter was built based on over 10 years of ERA5 data (from October 2007 to December 2018). The origin of the input par

Table 3-18: Summary of the origin of the ANNI input parameters for NH₃.

	Near-real time	Reanalysis
HRI	Calculated from L1C	Calculated from L1C
Satellite viewing angle	L1C	L1C
Surface emissivity	Zhou et al., (2013)	Zhou et al., (2013)
Atmospheric T and H ₂ O	IASI L2	ERA5
Surface pressure	IASI L2	ERA5
Skin temperature	IASI L2	Dedicated NN
Spread of the NH ₃ profile (σ) over ocean	0.9 km	0.9 km
Spread of the NH ₃ profile (σ) over land	ERA5 PBL climatology	ERA5
Peak NH ₃ altitude (z_0) over ocean	1.4 km	1.4 km
Peak NH ₃ altitude (z_0) over land	Surface height	Surface height



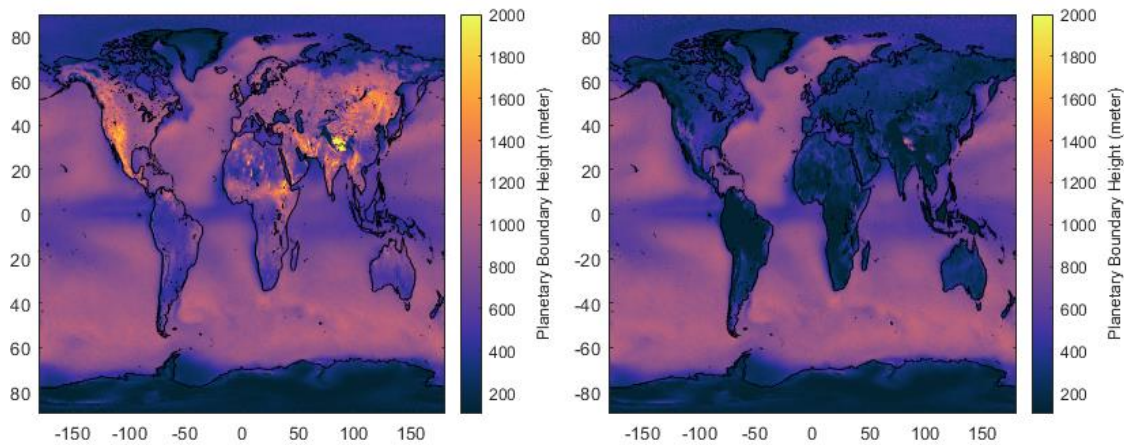


Figure 3-17: Example ERA5 climatology of the planetary boundary layer for April, morning (left) and evening (right).

Uncertainty

In the ANNI retrieval framework, per pixel uncertainty is calculated via propagation of uncertainty of the input parameters, allowing the discrimination of random and systematic uncertainties, with and without consideration of uncertainty related to the vertical profile. The treatment of uncertainties is detailed in the End-to-End ECV Uncertainty Budget (E3UB) document (D2.2).

Post filtering

As the retrieval does not use an a priori, it is poorly constrained in case of low sensitivity. Fortunately, the corresponding measurements can quite readily be filtered out. The post-filter flags retrievals with limited or no sensitivity to the measured quantity

$$\frac{1}{|\text{SF}|} > 1.5 \cdot 10^{16} \text{ molec.cm}^{-2}$$

and retrievals whose HRIs are either too noisy or for which the assumed vertical profile is incompatible with the measured HRI:

$$|\text{HRI}| > 1.5 \quad \text{and} \quad \hat{X}^a < 0.$$

Note on negative columns

The retrieval, by construction can return negative columns (inherited from negative HRIs and the fact that the neural network outputs the HRI-to-column ratios). While these clearly lack a clear physical interpretation, they are an integral part of the product and are not meant to be removed systematically. The use of negative physical quantities in satellite data is not new. They can for instance be found in MODIS AOD data starting from the Collection 5 (Levy et al., 2007). In this paper the authors call such negative values “statistically imperative” for creating an unbiased data set. For IASI observations of NH₃, which are expected to be measurable only in part of the data (i.e., in large areas and or certain periods, the retrieval should ideally average to 0), the necessity of having negative retrievals for an unbiased product becomes





even more important. Our retrieval setup deals automatically and in a natural way with the instrumental noise through the output of HRI-to-column ratios. As long as the HRI's are unbiased, an unbiased product is guaranteed, and the NN does not need to worry about instrumental noise and can assume that the measurements are noise-free.

It is however recommended to remove negative columns from time or space averaged data (an average over a large area, or a seasonal average), as these are not expected to exhibit important negative columns on average.

3.6.6. Examples

Single overpass

Example retrievals of the columns and associated uncertainties are shown in Figure 3-18 for a morning and evening overpass over Europe respectively. In the morning overpass, thanks to a good thermal contrast, the post filter does not remove many observations (apart from a few large negative ones). This contrasts with the evening overpass, where most observations are removed because of lack of sensitivity.

Seasonal climatology

An NH₃ seasonal climatology, based over 15 years of IASI measurements is shown in Figure 3-19.

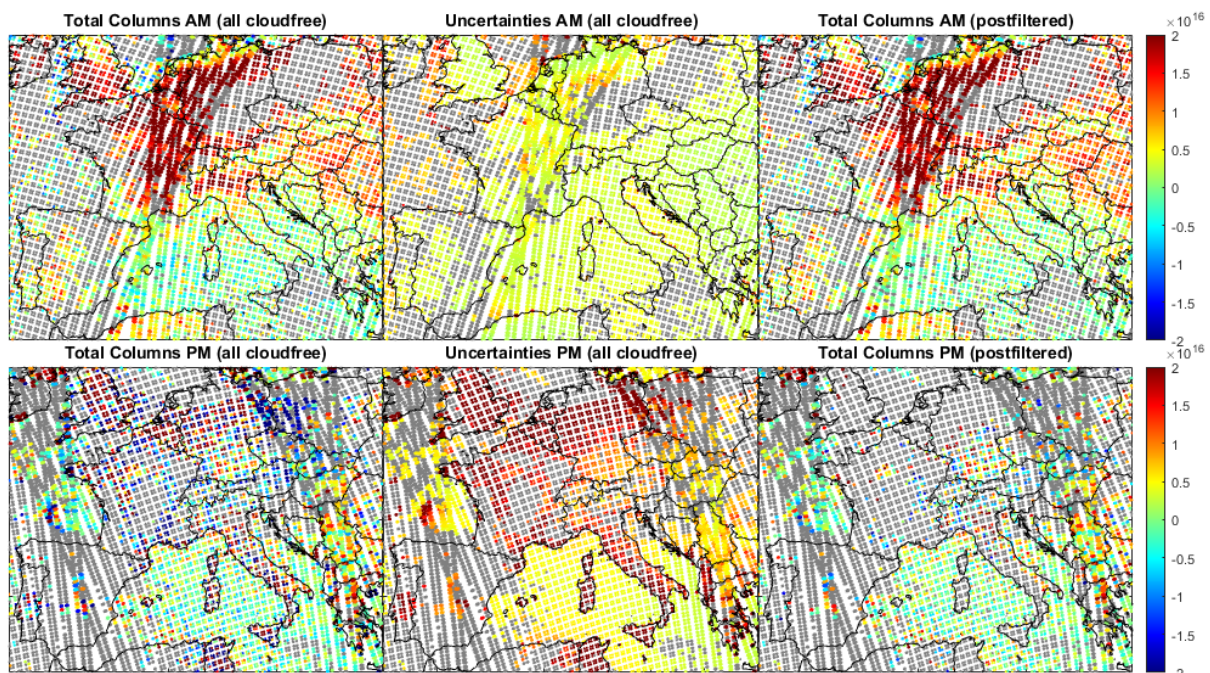


Figure 3-18: Example NH₃ retrievals from IASI-B on 24 April 2020 (AM, top; PM, bottom). Grey pixels are either cloudy or pixels that do not pass the post filter.

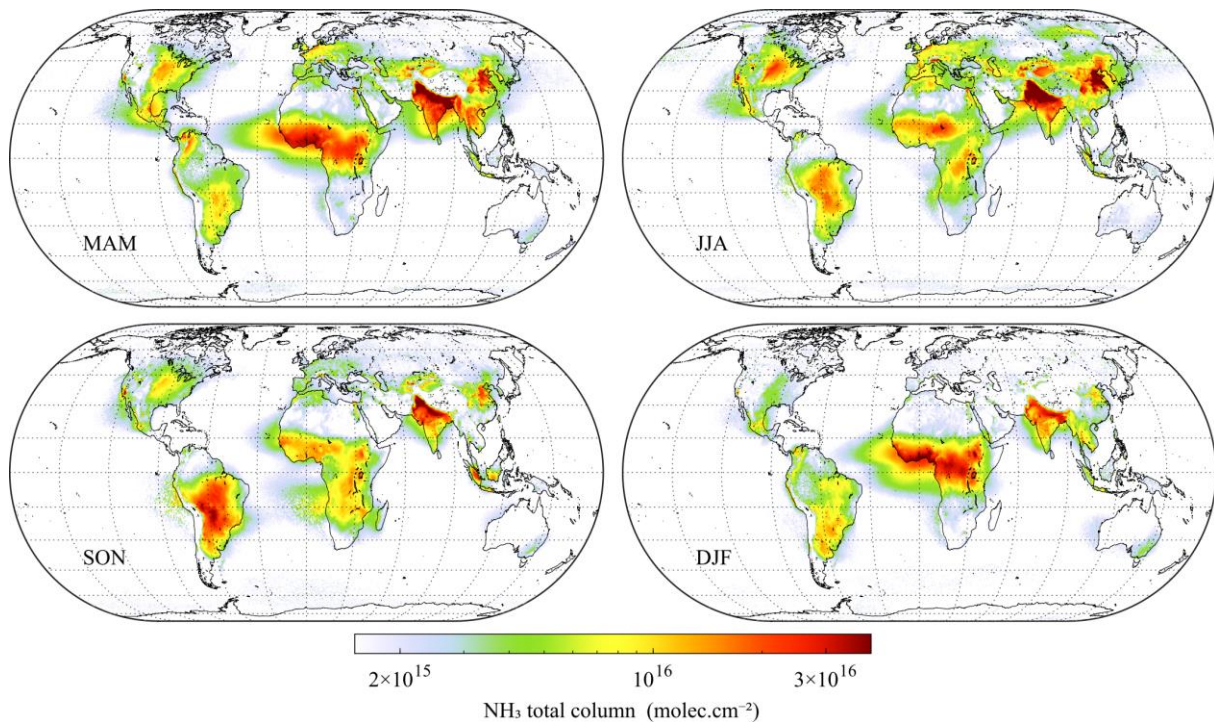


Figure 3-19: NH₃ seasonal average, derived from 0.5° by 0.5° monthly averages of the reanalysis product of ANNI v4. Data includes all measurements from IASI-A (October 2007 to December 2019), IASI-B (March 2013 to September 2022) and IASI-C (September 2019 to September 2022), with a cloud fraction below 10 %.

3.6.7. Advantages of the retrieval algorithm

Computational Efficiency. The only parameter retained from the measurement is the HRI value. Calculating these is straightforward and computational time is negligible. Calculating the neural network function is equally straightforward.

Full Spectral Range. The HRI takes into account a wide spectral range, which contains all the important NH₃ lines in the infrared, and thereby takes full advantage of the thermal infrared.

Low Dependency on the Forward Model. The forward model is only of secondary importance for the calculation of the Jacobians in the HRI and for the HRI calculated from the NN training data.

No A Priori Information. No a priori information on the column is used. This means that all the information from the final measurement comes from the spectral measurement (but potentially with very large associated uncertainties). Therefore, in contrast to optimal estimation approaches, no averaging kernel needs to be applied when carrying out comparison with other measurements/models. A priori information on the vertical profile shape is used but can be undone with averaging kernels.

Full Atmospheric State. Because the number of input parameters is not limited in the NN, the full temperature, humidity, and pressure profiles can be taken into account. This property is shared with the spectral fitting approaches.



Full Uncertainty Analysis. By perturbing the input parameters, a full uncertainty characterization can be made of how the uncertainty of each of the input parameters propagates to the final result. This analysis can be carried out on a per-pixel basis and allows separating of systematic and random uncertainty contributions.

Reduced Bias. Rather than mapping the input parameters directly to a NH_3 column, the output of the NN is a scaling factor, which after multiplication with the HRI gives the column. In this way, the instrumental error on the HRI is translated in a linear way in an error on the column, and negative columns become possible. At the same time, this implies that the algorithm itself is relatively unbiased by design (this is assuming that the HRI values are not biased).

3.6.8. Comparison with an OEM retrieval

Here, we present the results of an independent intercomparison that was conducted between the ANNI v4 retrieval output and that of an optimal estimation approach which relies on spectral fitting.

For the optimal estimation retrieval, the Atmosphit forward and inverse model was used (Coheur et al., 2005), which is the same tool whose forward model is used for the construction of the ANNI training database. The optimal estimation was set up as follows. The retrieval range was set to 900 to 975 cm^{-1} . Total columns of NH_3 were retrieved with a fixed vertical profile, using the same parametrization as in ANNI NRT. The NH_3 variance was set to 1000%, corresponding to an almost unconstrained retrieval. Together with NH_3 , H_2O was retrieved in 10 partial columns, with the a priori coming from the IASI L2. Total columns of CO_2 , O_3 and CFC-12 were retrieved as well as the surface temperature. Spectral emissivity was taken from Zhou et al. (2013). Before presenting the results, it should be emphasized that despite the similarities in both retrieval approaches (same input parameters, vertical profiles, forward model), no perfect agreement is expected because of: (1) use of a narrower spectral range in the optimal estimation retrieval; (2) different propagation of instrumental noise to the retrieval result; (3) limitations of the fitting model (e.g. with respect to fitting water vapour or surface emissivity); (4) errors related to the imperfect training of the neural network.

For the comparison, two days were selected, one over Europe and one over North America, with relatively high NH_3 columns. The results are shown in Figure 3-20. Intercepts, mean, and median differences are all in the order of 10^{15} molec. cm^{-2} or below. Regression slopes, calculated using iteratively reweighted least squares to remove the impact of outliers, are 0.97 and 1.05. While the scatter around the 1--1 lines is not negligible (with standard deviation of the differences around 3-4 10^{15} molec. cm^{-2}), these numbers demonstrate the overall consistency of both retrieval approaches and do not indicate a significant bias.

The last detailed global validation of the IASI NH_3 product was based on a comparison of ground-based FTIR measurements of NH_3 with the LUT-based NH_3 product, where a low bias around 35% was found (Dammers et al., 2016). Since then, two independent validation studies have been conducted. One study (Guo et al., 2021) compared IASI ANNI v3 with in situ measurements in Colorado, U.S. and found regression slopes ranging from 0.78 to 1.1, and intercepts of the order of 1 to 2 10^{15} molec. cm^{-2} . A second study (Wang et al., 2020) compared

IASI NH₃ columns with columns obtained from FTIR measurements in Hefei, China. Here, mean differences around 3.5×10^{15} molec.cm⁻² (IASI being lower) were found and regression slopes close to one. Given the results of the comparison with the optimal estimation method, we do not expect any significant bias in ANNI v4 for columns above 10^{16} molec.cm⁻² in comparisons that correct for the vertical profile assumption of the retrieval.

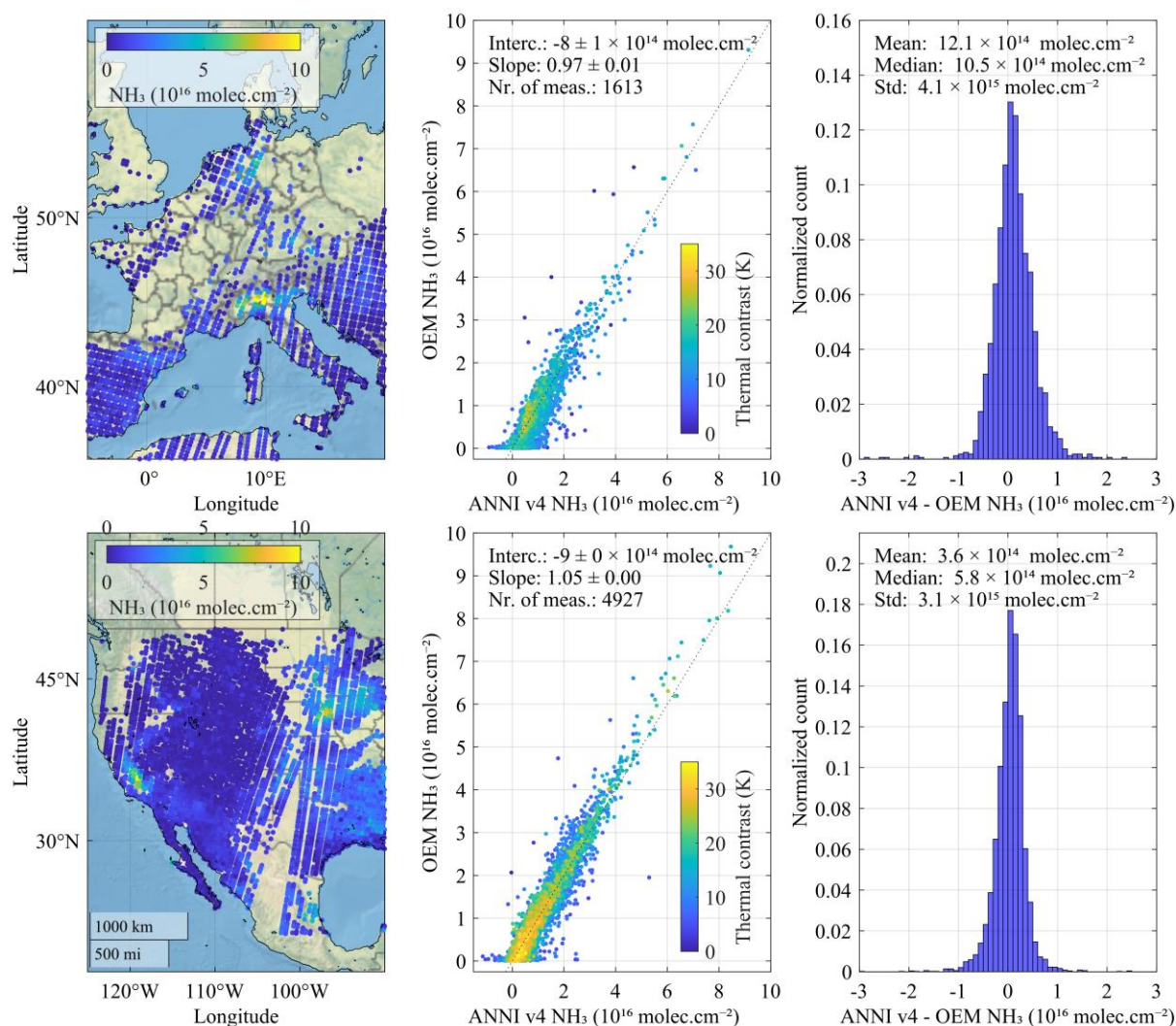


Figure 3-20: Comparison between ANNI v4 NH₃ columns and retrievals based on optimal estimation for two scenes, one over Europe (top panels, 18 April 2013, Metop A morning overpass) and North America (bottom panels, 6 May 2021, Metop B morning overpass). The left panels depict the optimal estimation retrieved columns. The middle panels are scatter plots between the two retrievals, where each observation is colour coded according to thermal contrast (brightness temperature of the surface minus the temperature at half the boundary layer height). The right panels summarize the comparison by means of histograms of the differences.





4. Level-3 algorithms

4.1. Tropospheric nitrogen dioxide (L3-NO₂)

4.1.1. Overview

4.1.2. Data gridding approach

4.1.3. Inter-sensor bias analysis

4.1.4. Data merging algorithm

4.1.5. Uncertainty estimate

4.2. Formaldehyde (L3-HCHO)

4.3. Sulfur dioxide (L3-SO₂)

4.4. Glyoxal (L3-CHOCHO)

4.5. Carbon monoxide (L3-CO)

4.6. Ammonia (L3-NH₃)

5. References

Alvarado, L. M. A., Richter, A., Vrekoussis, M., Wittrock, F., Hilboll, A., Schreier, S. F. and Burrows, J. P.: An improved glyoxal retrieval from OMI measurements, *Atmos. Meas. Tech.*, 7(12), 4133–4150, doi:10.5194/amt-7-4133-2014, 2014.

August, T., Klaes, D., Schlüssel, P., Hultberg, T., Crapeau, M., Arriaga, A., O'Carroll, A., Coppens, D., Munro, R., & Calbet, X. (2012) IASI on Metop-A: Operational Level 2 retrievals after five years in orbit. *Journal of Quantum Spectroscopy and Radiative Transfer* 113, 1340–1371.

Barkley, M. P., González Abad, G., Kurosu, T. P., Spurr, R., Torbatian, S., and Lerot, C.: OMI air-quality monitoring over the Middle East, *Atmos. Chem. Phys.*, 17, 4687–4709, <https://doi.org/10.5194/acp-17-4687-2017>, 2017



-
- Beirle, S., Hörmann, C., Jöckel, P., Liu, S., Penning de Vries, M., Pozzer, A., Sihler, H., Valks, P., and Wagner, T.: The STRatospheric Estimation Algorithm from Mainz (STREAM): estimating stratospheric NO₂ from nadir-viewing satellites by weighted convolution, *Atmos. Meas. Tech.*, 9, 2753–2779, <https://doi.org/10.5194/amt-9-2753-2016>, 2016.
- Beirle, S., Sihler, H., and Wagner, T.: Linearisation of the effects of spectral shift and stretch in DOAS analysis, *Atmos. Meas. Tech.*, 6, 661–675, <https://doi.org/10.5194/amt-6-661-2013>, 2013.
- Boersma, K. F., Eskes, H. J., and Brinksma, E. J.: Error analysis for tropospheric NO₂ retrieval from space, *J. Geophys. Res.*, 109, D04311, doi: 10.1029/2003JD003962, 2004.
- Boersma, K. F., Eskes, H. J., Dirksen, R. J., van der A, R. J., Veefkind, J. P., Stammes, P., Huijnen, V., Kleipool, Q. L., Sneep, M., Claas, J., Leitão, J., Richter, A., Zhou, Y., and Brunner, D.: An improved tropospheric NO₂ column retrieval algorithm for the Ozone Monitoring Instrument, *Atmos. Meas. Tech.*, 4, 1905–1928, <https://doi.org/10.5194/amt-4-1905-2011>, 2011.
- Boersma, K. F., Eskes, H. J., Richter, A., De Smedt, I., Lorente, A., Beirle, S., van Geffen, J. H. G. M., Zara, M., Peters, E., Van Roozendaal, M., Wagner, T., Maasakkers, J. D., van der A, R. J., Nightingale, J., De Rudder, A., Irie, H., Pinardi, G., Lambert, J.-C., and Compernolle, S. C.: Improving algorithms and uncertainty estimates for satellite NO₂ retrievals: results from the quality assurance for the essential climate variables (QA4ECV) project, *Atmos. Meas. Tech.*, 11, 6651–6678, <https://doi.org/10.5194/amt-11-6651-2018>, 2018.
- Bogumil, K., Orphal, J., Homann, T., Voigt, S., Spietz, P., Fleischmann, O., Vogel, A., Hartmann, M., Bovensmann, H., Frerick, J., and Burrows, J.P.: Measurements of molecular absorption spectra with the SCIAMACHY Pre-Flight Model: instrument characterization and reference data for atmospheric remote-sensing in the 230-2380 nm region, *Journal of Photochemistry and Photobiology A*, 157, 167-184, 2003.
- Camy-Peyret, C., & Eyre, J. (1998). The IASI Science Plan. Technical report, A Report From The IASI Sounding Science Working Group.
- Chan Miller, C., Gonzalez Abad, G., Wang, H., Liu, X., Kurosu, T., Jacob, D. J. and Chance, K.: Glyoxal retrieval from the Ozone Monitoring Instrument, *Atmos. Meas. Tech.*, 7(11), 3891–3907, doi:10.5194/amt-7-3891-2014, 2014.
- Clarisse, L., Clerbaux, C., Franco, B., Hadji-Lazaro, J., Whitburn, S., Kopp, A. K., Hurtmans, D., and Coheur, P.-F.: A Decadal Data Set of Global Atmospheric Dust Retrieved From IASI Satellite Measurements, *J. Geophys. Res. Atmos.*, 124, 1618–1647, <https://doi.org/10.1029/2018jd029701>, 2019.
- Clarisse, L., Coheur, P. F., Prata, F., Hadji-Lazaro, J., Hurtmans, D., & Clerbaux, C. (2013). A unified approach to infrared aerosol remote sensing and type specification. *Atmospheric Chemistry and Physics*, 13(4), 2195-2221.
- Clarisse, L., Franco, B., Van Damme, M., Di Gioacchino, T., Hadji-Lazaro, J., Whitburn, S., Noppen, L., Hurtmans, D., Clerbaux, C., and Coheur, P.: The IASI NH₃ version 4 product: averaging kernels and improved consistency, *Atmos. Meas. Tech. Discuss.* [preprint], <https://doi.org/10.5194/amt-2023-48>, in review, 2023.
- Clerbaux, C., Boynard, A., Clarisse, L., George, M., Hadji-Lazaro, J., Herbin, H., Hurtmans, D., Pommier, M., Razavi, A., Turquety, S., Wespes, C., & Coheur, P.-F.: Monitoring of atmospheric composition





using the thermal infrared IASI/MetOp sounder. *Atmospheric Chemistry and Physics*, 9, 6041–6054, 2009.

Coheur, P.-F., Barret, B., Turquety, S., Hurtmans, D., Hadji-Lazaro, J., and Clerbaux, C.: Retrieval and characterization of ozone vertical profiles from a thermal infrared nadir sounder, *J. Geophys. Res.*, 110, D24 303, <https://doi.org/10.1029/2005JD005845>, 2005.

Compernelle, S., Verhoelst, T., Pinardi, G., Granville, J., Hubert, D., Keppens, A., ... & Lambert, J. C. (2020). Validation of Aura-OMI QA4ECV NO₂ climate data records with ground-based DOAS networks: the role of measurement and comparison uncertainties. *Atmospheric Chemistry and Physics*, 20(13), 8017-8045.

Dammers, E., Palm, M., Damme, M. V., Vigouroux, C., Smale, D., Conway, S., Toon, G. C., Jones, N., Nussbaumer, E., Warneke, T., Petri, C., Clarisse, L., Clerbaux, C., Hermans, C., Lutsch, E., Strong, K., Hannigan, J. W., Nakajima, H., Morino, I., Herrera, B., Stremme, W., Grutter, M., Schaap, M., Kruit, R. J. W., Notholt, J., Coheur, P.-F., and Erisman, J. W.: An evaluation of IASI-NH 3 with ground-based Fourier transform infrared spectroscopy measurements, *Atmos. Chem. Phys.*, 16, 10 351–10 368, <https://doi.org/10.5194/acp-16-10351-2016>, 2016

Danckaert, T., Fayt, C., van Roozendaal, M., De Smedt, I., Letocard, V., Merlaud, A. and Pinardi, G.: QDOAS software user manual. [online] Available from: http://uv-vis.aeronomie.be/software/QDOAS/QDOAS_manual.pdf, 2017

De Smedt, I., Pinardi, G., Vigouroux, C., Compernelle, S., Bais, A., Benavent, N., Boersma, F., Chan, K.-L., Donner, S., Eichmann, K.-U., Hedelt, P., Hendrick, F., Irie, H., Kumar, V., Lambert, J.-C., Langerock, B., Lerot, C., Liu, C., Loyola, D., Piders, A., Richter, A., Rivera Cárdenas, C., Romahn, F., Ryan, R. G., Sinha, V., Theys, N., Vlietinck, J., Wagner, T., Wang, T., Yu, H., and Van Roozendaal, M.: Comparative assessment of TROPOMI and OMI formaldehyde observations and validation against MAX-DOAS network column measurements, *Atmos. Chem. Phys.*, 21, 12561–12593, <https://doi.org/10.5194/acp-21-12561-2021>, 2021.

De Smedt, I., Theys, N., van Gent, J., Danckaert, T., Yu, H., and Van Roozendaal, M.: S5P/TROPOMI HCHO ATBD, S5P-BIRA-L2-400F-ATBD, v2.4.1, 2022-06-22, Level-2 Algorithm Developments for Sentinel-5 Precursor.

De Smedt, I., Theys, N., Yu, H., Danckaert, T., Lerot, C., Compernelle, S., Van Roozendaal, M., Richter, A., Hilboll, A., Peters, E., Pedergrana, M., Loyola, D., Beirle, S., Wagner, T., Eskes, H., van Geffen, J., Boersma, K. F., and Veefkind, P.: Algorithm theoretical baseline for formaldehyde retrievals from S5P TROPOMI and from the QA4ECV project, *Atmos. Meas. Tech.*, 11, 2395–2426, <https://doi.org/10.5194/amt-11-2395-2018>, 2018.

De Smedt, I., Yu, H., Richter, A., Beirle, S., Eskes, H., Boersma, K. F., Van Roozendaal, M., Van Geffen, J., Lorente, A., and Peters, E.: QA4ECV HCHO tropospheric column data from OMI (Version 1.1) [Data set], Royal Belgian Institute for Space Aeronomy, <https://doi.org/10.18758/71021031>, 2017.

Dirksen, R. J., Boersma, K. F., Eskes, H. J., Ionov, D. V., Bucsel, E. J., Levelt, P. F., and Kelder, H. M.: Evaluation of stratospheric NO₂ retrieved from the Ozone Monitoring Instrument: Intercomparison, diurnal cycle, and trending, *J. Geophys. Res.*, 116, D08305, [doi:10.1029/2010JD014943](https://doi.org/10.1029/2010JD014943), 2011.



Eaton, M.: Multivariate Statistics: A Vector Space Approach, Institute of Mathematical Statistics, Beachwood, Ohio, USA, 2007.

Eskes, H. J. and K. F. Boersma, Averaging kernels for DOAS total-column satellite retrievals, *Atmos. Chem. Phys.*, 3, 1285-1291, 2003.

Franco, B., Clarisse, L., Stavrakou, T., Müller, J.-F., Van Damme, M., Whitburn, S., Hadji-Lazaro, J., Hurtmans, D., Taraborrelli, D., Clerbaux, C., and Coheur, P.-F.: A General Framework for Global Retrievals of Trace Gases From IASI: Application to Methanol, Formic Acid, and PAN, *J. Geophys. Res. Atmos.*, 123, 13,963–13,984, <https://doi.org/10.1029/2018jd029633>, 2018.

Georgoulias, A. K., van der A, R. J., Stammes, P., Boersma, K. F., and Eskes, H. J.: Trends and trend reversal detection in 2 decades of tropospheric NO₂ satellite observations, *Atmos. Chem. Phys.*, 19, 6269–6294, <https://doi.org/10.5194/acp-19-6269-2019>, 2019.

Guo, X., Clarisse, L., Wang, R., Van Damme, M., Whitburn, S., Coheur, P.-F., Clerbaux, C., Franco, B., Pan, D., Golston, L. M., Wendt, L., Sun, K., Tao, L., Miller, D., Mikoviny, T., Müller, M., Wisthaler, A., Tevlin, A. G., Murphy, J. G., Nowak, J. B., Roscioli, J. R., Volkamer, R., Kille, N., Neuman, J. A., Eilerman, S. J., Crawford, J. H., Yacovitch, T. I., Barrick, J. D., Scarino, A. J., and Zondlo, M. A.: Validation of IASI satellite ammonia observations at the pixel scale using in-situ vertical profiles, *J. Geophys. Res. Atmos.*, <https://doi.org/10.1029/2020jd033475>, 2021.

Hermans, C., Vandaele, A.C., and Fally, S.: Fourier transform measurements of SO₂ absorption cross sections: I. Temperature dependence in the 24 000–29 000 cm⁻¹ (345–420 nm) region, *J. Quant Spectrosc. Radiat. Transfer*, 110, 756–765, doi: 10.1016/j.jqsrt.2009.10.031, 2009.

Hersbach, H., Bell, B., Berrisford, P., Hirahara, S., Horányi, A., Muñoz-Sabater, J., Nicolas, J., Peubey, C., Radu, R., Schepers, D., Simmons, A., Soci, C., Abdalla, S., Abellan, X., Balsamo, G., Bechtold, P., Biavati, G., Bidlot, J., Bonavita, M., Chiara, G., Dahlgren, P., Dee, D., Diamantakis, M., Dragani, R., Flemming, J., Forbes, R., Fuentes, M., Geer, A., Haimberger, L., Healy, S., Hogan, R. J., Hólm, E., Janisková, M., Keeley, S., Laloyaux, P., Lopez, P., Lupu, C., Radnoti, G., Rosnay, P., Rozum, I., Vamborg, F., Villaume, S., and Thépaut, J.-N.: The ERA5 global reanalysis, *Q. J. R. Meteorolog. Soc.*, 146, 1999–2049, <https://doi.org/10.1002/qj.3803>, 2020.

Hilton, F., August, T., Barnet, C., Bouchard, A., Camy-Peyret, C., Clarisse, L., Clerbaux, C., Coheur, P.-F., Collard, A., Crevoisier, C., Dufour, G., Edwards, D., Faijan, F., Fourrié, N., Gambacorta, A., Gauguin, S., Guidard, V., Hurtmans, D., Illingworth, S., Jacquinet-Husson, N., Kerzenmacher, T., Klaes, D., Lavanant, L., Masiello, G., Matricardi, M., McNally, T., Newman, S., Pavelin, E., Péquignot, E., Phulpin, T., Remedios, J., Schlüssel, P., Serio, C., Strow, L., Taylor, J., Tobin, D., Uspensky, A., & Zhou, D. (2012). Hyperspectral Earth Observation with IASI. *Bulletin of the American Meteorological Society*, 93(3), 347-370.

Kleipool, Q. L., Dobber, M. R., de Haan, J. F. and Levelt, P. F.: Earth surface reflectance climatology from 3 years of OMI data, *J. Geophys. Res.*, 113(D18), D18308, doi:10.1029/2008JD010290, 2008.

Kleipool, Q., Rozemeijer, N., van Hoek, M., Leloux, J., Loots, E., Ludewig, A., van der Plas, E., Adrichem, D., Harel, R., Spronk, S., ter Linden, M., Jaross, G., Haffner, D., Veeffkind, P., and Levelt, P. F.: Ozone Monitoring Instrument (OMI) collection 4: establishing a 17-year-long series of detrended level-1b data, *Atmos. Meas. Tech.*, 15, 3527–3553, <https://doi.org/10.5194/amt-15-3527-2022>, 2022.





-
- Lerot, C., Stavrakou, T., Van Roozendael, M., Alvarado, L.M.A. and Richter, A.: GLYoxal Retrievals from TROPOMI (GLYRETRO) – ATBD, 2021, available at https://data-portal.s5p-pal.com/product-docs/chocho/CHOCHO_ATBD_S5P+I_BIRA_v3.1.pdf
- Lerot, C., Stavrakou, T., De Smedt, I., Müller, J. F., Van Roozendael, M., Müller, J. F. and Van Roozendael, M.: Glyoxal vertical columns from GOME-2 backscattered light measurements and comparisons with a global model, *Atmos. Chem. Phys.*, 10(24), 12059–12072, doi:10.5194/acp-10-12059-2010, 2010.
- Levy, R. C., Remer, L. A., Mattoo, S., Vermote, E. F., & Kaufman, Y. J. : Second-generation operational algorithm: Retrieval of aerosol properties over land from inversion of Moderate Resolution Imaging Spectroradiometer spectral reflectance. *Journal of Geophysical Research: Atmospheres*, 112(D13), 2007.
- Liu, S., Valks, P., Pinardi, G., De Smedt, I., Yu, H., Beirle, S., and Richter, A.: An improved total and tropospheric NO₂ column retrieval for GOME-2, *Atmos. Meas. Tech.*, 12, 1029–1057, <https://doi.org/10.5194/amt-12-1029-2019>, 2019.
- Liu, S., Valks, P., Pinardi, G., Xu, J., Argyrouli, A., Lutz, R., Tilstra, L. G., Huijnen, V., Hendrick, F., and Van Roozendael, M.: An improved air mass factor calculation for nitrogen dioxide measurements from the Global Ozone Monitoring Experiment-2 (GOME-2), *Atmos. Meas. Tech.*, 13, 755–787, <https://doi.org/10.5194/amt-13-755-2020>, 2020.
- Lorente, A., Folkert Boersma, K., Yu, H., Dörner, S., Hilboll, A., Richter, A., Liu, M., Lamsal, L. N., Barkley, M., De Smedt, I., Van Roozendael, M., Wang, Y., Wagner, T., Beirle, S., Lin, J.-T., Krotkov, N., Stammes, P., Wang, P., Eskes, H. J., and Krol, M.: Structural uncertainty in air mass factor calculation for NO₂ and HCHO satellite retrievals, *Atmos. Meas. Tech.*, 10, 759–782, <https://doi.org/10.5194/amt-10-759-2017>, 2017.
- Loyola, D. G., Gimeno García, S., Lutz, R., Argyrouli, A., Romahn, F., Spurr, R. J. D., Pedernana, M., Doicu, A., Molina García, V., and Schüssler, O.: The operational cloud retrieval algorithms from TROPOMI on board Sentinel-5 Precursor, *Atmos. Meas. Tech.*, 11, 409–427, <https://doi.org/10.5194/amt-11-409-2018>, 2018.
- Lutz, R., Loyola, D., Gimeno García, S., and Romahn, F.: OCRA radiometric cloud fractions for GOME-2 on MetOp-A/B, *Atmos. Meas. Tech.*, 9, 2357–2379, <https://doi.org/10.5194/amt-9-2357-2016>, 2016.
- Martin, R. V., et al., An improved retrieval of tropospheric nitrogen dioxide from GOME, *J. Geophys. Res.*, 107(D20), 4437, doi:10.1029/2001JD001027, 2002.
- Oldeman, A. M.: Effect of including an intensity offset in the DOAS NO₂ retrieval of TROPOMI, Internship report, R-1944-SE, Eindhoven University of Technology, Eindhoven, The Netherlands, 2018.
- Palmer, P. I., Jacob, D. J., Chance, K. V., Martin, R. V., D, R. J., Kurosu, T. P., Bey, I., Yantosca, R. and Fiore, A.: Air mass factor formulation for spectroscopic measurements from satellites: Application to formaldehyde retrievals from the Global Ozone Monitoring Experiment, *Journal of Geophysical Research*, 106(D13), 14539-14550, doi:10.1029/2000JD900772, 2001.





Puķīte, J., Kühl, S., Deutschmann, T., Platt, U. and Wagner, T.: Extending differential optical absorption spectroscopy for limb measurements in the UV, *Atmos. Meas. Tech.*, 3(3), 631–653, doi:10.5194/amt-3-631-2010, 2010.

Richter, A.: qa4ecv_no2_inhomogeneous_scenes_171221, in QA4ECV technical note, Treatment of inhomogeneous scenes., 2018.

Rodgers, C. D. and Connor, B. J.: Intercomparison of remote sounding instruments, *J. Geophys. Res.*, 108, <https://doi.org/10.1029/2002JD002299>, 2003.

Rodgers, C. D.: *Inverse Methods for Atmospheric Sounding, Theory and Practice*, World Scientific Publishing, Singapore-New-Jersey-London-Hong Kong, 2000.

Seo, S., Valks, P., Boersma, K. F., De Smedt, I., Pinardi, G., Liu, S., Richter, A., and Loyola, D.: Development and evaluation of a long-term NO₂ data record from GOME-2 observations, in preparation, 2023.

Theys, N. et al., S5P/TROPOMI SO₂ ATBD, 2023. Available at: <https://sentinel.esa.int/web/sentinel/technical-guides/sentinel-5p/products-algorithms>.

Theys, N., De Smedt, I., Yu, H., Danckaert, T., van Gent, J., Hörmann, C., Wagner, T., Hedelt, P., Bauer, H., Romahn, F., Pedergrana, M., Loyola, D. and Van Roozendael, M.: Sulfur dioxide retrievals from TROPOMI onboard Sentinel-5 Precursor: algorithm theoretical basis, *Atmos. Meas. Tech.*, 10(1), 119–153, doi:10.5194/amt-10-119-2017, 2017.

Theys, N., Fioletov, V., Li, C., De Smedt, I., Lerot, C., McLinden, C., Krotkov, N., Griffin, D., Clarisse, L., Hedelt, P., Loyola, D., Wagner, T., Kumar, V., Innes, A., Ribas, R., Hendrick, F., Vlietinck, J., Brenot, H., and Van Roozendael, M.: A sulfur dioxide Covariance-Based Retrieval Algorithm (COBRA): application to TROPOMI reveals new emission sources, *Atmos. Chem. Phys.*, 21, 16727–16744, <https://doi.org/10.5194/acp-21-16727-2021>, 2021.

Theys, N., Lerot, C., Brenot, H., van Gent, J., Smedt, I. D., Clarisse, L., Burton, M., Varnam, M., Hayer, C., Esse, B., and Van Roozendael, M.: Improved retrieval of SO₂ plume height from TROPOMI using an iterative Covariance-Based Retrieval Algorithm, *Atmos. Meas. Tech.*, 15, 4801–4817, <https://doi.org/10.5194/amt-15-4801-2022>, 2022.

Tilstra, L. G., Tuinder, O. N. E., Wang, P., and Stammes, P.: Directionally dependent Lambertian-equivalent reflectivity (DLER) of the Earth's surface measured by the GOME-2 satellite instruments, *Atmos. Meas. Tech.*, 14, 4219–4238, <https://doi.org/10.5194/amt-14-4219-2021>, 2021.

Tilstra, L.G., TROPOMI ATBD of the directionally dependent surface Lambertian-equivalent reflectivity, KNMI Report S5P-KNMI-L3-0301-RP, Issue 2.1.0, September 4, 2023.

Valks, P., Chan, L., Hedelt, P., Slijkhuis, S., and Lutz, R.: Algorithm Theoretical Basis Document for GOME-2 Total Column Products of Ozone, NO₂, BrO, SO₂, H₂O, HCHO and Cloud Properties (GDP 4.8 for GOME-2 on MetOp-A and B, GDP 4.9 for GOME-2 on MetOp-C), Tech. rep., SAF/AC/DLR/ATBD/01, Iss./Rev.: 3/B, 2019.

Van Damme, M., Clarisse, L., Franco, B., Sutton, M. A., Erisman, J. W., Kruit, R. W., van Zanten, M., Whitburn, S., Hadji-Lazaro, J., Hurtmans, D., Clerbaux, C., and Coheur, P.-F.: Global, regional and national trends of atmospheric ammonia derived from a decadal (2008–2018) satellite record, *Environ. Res. Lett.*, <https://doi.org/10.1088/1748-9326/abd5e0>, 2021.





-
- Van Damme, M., Whitburn, S., Clarisse, L., Clerbaux, C., Hurtmans, D., and Coheur, P.-F.: Version 2 of the IASI NH 3 neural network retrieval algorithm: near-real-time and reanalysed datasets, *Atmos. Meas. Tech.*, 10, 4905–4914, <https://doi.org/10.5194/amt-10-4905-2017>, 2017.
- van Geffen, J. H. G. M., Eskes, H. J., Boersma, K. F., and Veefkind, J. P.: TROPOMI ATBD of the total and tropospheric NO₂ data products, Tech. Rep. S5P-KNMI-L2-0005-RP, Koninklijk Nederlands Meteorologisch Instituut (KNMI), <https://sentinels.copernicus.eu/documents/247904/2476257/Sentinel-5P-TROPOMI-ATBD-NO2-data-products>, CI-7430-ATBD, issue 2.2.0, 16 June 2021.
- van Geffen, J., Boersma, K. F., Eskes, H., Sneep, M., ter Linden, M., Zara, M., and Veefkind, J. P.: S5P TROPOMI NO₂ slant column retrieval: method, stability, uncertainties and comparisons with OMI, *Atmos. Meas. Tech.*, 13, 1315–1335, <https://doi.org/10.5194/amt-13-1315-2020>, 2020.
- van Geffen, J., Eskes, H., Compernelle, S., Pinardi, G., Verhoelst, T., Lambert, J.-C., Sneep, M., ter Linden, M., Ludewig, A., Boersma, K. F., and Veefkind, J. P.: Sentinel-5P TROPOMI NO₂ retrieval: impact of version v2.2 improvements and comparisons with OMI and ground-based data, *Atmos. Meas. Tech.*, 15, 2037–2060, <https://doi.org/10.5194/amt-15-2037-2022>, 2022.
- Verhoelst, T., Compernelle, S., Pinardi, G., Lambert, J.-C., Eskes, H. J., Eichmann, K.-U., Fjæraa, A. M., Granville, J., Niemeijer, S., Cede, A., Tiefengraber, M., Hendrick, F., Pazmiño, A., Bais, A., Bazureau, A., Boersma, K. F., Bogner, K., Dehn, A., Donner, S., Elokhov, A., Gebetsberger, M., Goutail, F., Grutter de la Mora, M., Gruzdev, A., Gratsea, M., Hansen, G. H., Irie, H., Jepsen, N., Kanaya, Y., Karagkiozidis, D., Kivi, R., Kreher, K., Levelt, P. F., Liu, C., Müller, M., Navarro Comas, M., PETERS, A. J. M., Pommereau, J.-P., Portafaix, T., Prados-Roman, C., Puentedura, O., Querel, R., Remmers, J., Richter, A., Rimmer, J., Rivera Cárdenas, C., Saavedra de Miguel, L., Sinyakov, V. P., Stremme, W., Strong, K., Van Roozendaal, M., Veefkind, J. P., Wagner, T., Wittrock, F., Yela González, M., and Zehner, C.: Ground-based validation of the Copernicus Sentinel-5P TROPOMI NO₂ measurements with the NDACC ZSL-DOAS, MAX-DOAS and Pandonia global networks, *Atmos. Meas. Tech.*, 14, 481–510, <https://doi.org/10.5194/amt-14-481-2021>, 2021.
- Volkamer, R., Baidar, S., Campos, T. L., Coburn, S., DiGangi, J. P., Dix, B., Eloranta, E. W., Koenig, T. K., Morley, B., Ortega, I., Pierce, B. R., Reeves, M., Sinreich, R., Wang, S., Zondlo, M. A. and Romashkin, P. A.: Aircraft measurements of BrO, IO, glyoxal, NO₂, H₂O, O₂–O₂ and aerosol extinction profiles in the tropics: comparison with aircraft-/ship-based in situ and lidar measurements, *Atmos. Meas. Tech.*, 8(5), 2121–2148, doi:10.5194/amt-8-2121-2015, 2015.
- Walker, J. C., Dudhia, A., and Carboni, E.: An effective method for the detection of trace species demonstrated using the MetOp Infrared Atmospheric Sounding Interferometer, *Atmos. Meas. Tech.*, 4, 1567–1580, <https://doi.org/10.5194/amt-4-1567-2011>, 2011.
- Wang, P., P. Stammes, R. van der A, G. Pinardi, and M. van Roozendaal, FRESCO+: an improved O₂ A-band cloud retrieval algorithm for tropospheric trace gas retrievals, *Atmos. Chem. Phys.*, 8, 6565–6576, doi:10.5194/acp-8-6565-2008, 2008.
- Wang, P., PETERS, A., van Geffen, J., Tuinder, O., Stammes, P., and Kinne, S.: Shipborne MAX-DOAS measurements for validation of TROPOMI NO₂ products, *Atmos. Meas. Tech.*, 13, 1413–1426, <https://doi.org/10.5194/amt-13-1413-2020>, 2020.
- Wang, W., Liu, C., Clarisse, L., Van Damme, M., Coheur, P.-F., Xie, Y., Shan, C., Hu, Q., Zhang, H., Sun, Y., Yin, H., and Jones, N.: Spatial distribution and seasonal variability in atmospheric ammonia





measured from ground-based FTIR observations at Hefei, China, *Atmos. Meas. Tech. Discuss.*, <https://doi.org/10.5194/amt-2020-39>, 2020.

Whitburn, S., Clarisse, L., Bouillon, M., Safi eddine, S., George, M., Dewitte, S., De Longueville, H., Coheur, P.-F., and Clerbaux, C.: Trends in spectrally resolved outgoing longwave radiation from 10 years of satellite measurements, *NPJ Clim. Atmos. Sci.*, 4, <https://doi.org/10.1038/s41612-021-00205-7>, 2021.

Whitburn, S., Clarisse, L., Crapeau, M., August, T., Hultberg, T., Coheur, P. F., and Clerbaux, C.: A CO₂-independent cloud mask from Infrared Atmospheric Sounding Interferometer (IASI) radiances for climate applications, *Atmos. Meas. Tech.*, 15, 6653–6668, <https://doi.org/10.5194/amt-15-6653-2022>, 2022.

Whitburn, S., Van Damme, M., Clarisse, L., Bauduin, S., Heald, C. L., Hadji-Lazaro, J., Hurtmans, D., Zondlo, M. A., Clerbaux, C., and Coheur, P.-F.: A flexible and robust neural network IASI-NH 3 retrieval algorithm, *J. Geophys. Res.*, 121, 6581–6599, <https://doi.org/10.1002/2016jd024828>, 2016.

Williams, J. E., Boersma, K. F., Le Sager, P., and Verstraeten, W. W.: The high-resolution version of TM5-MP for optimized satellite retrievals: description and validation, *Geosci. Model Dev.*, 10, 721–750, doi:10.5194/gmd-10-721-2017, 2017.

Zara, M., Boersma, K. F., De Smedt, I., Richter, A., Peters, E., van Geffen, J. H. G. M., Beirle, S., Wagner, T., Van Roozendaal, M., Marchenko, S., Lamsal, L. N., and Eskes, H. J.: Improved slant column density retrieval of nitrogen dioxide and formaldehyde for OMI and GOME-2A from QA4ECV: intercomparison, uncertainty characterisation, and trends, *Atmos. Meas. Tech.*, 11, 4033–4058, <https://doi.org/10.5194/amt-11-4033-2018>, 2018.

Zhou, D. K., Larar, A. M., and Liu, X.: MetOp-A/IASI Observed Continental Thermal IR Emissivity Variations, *IEEE J. Sel. Topics Appl. Earth Observations Remote Sens.*, 6, 1156–1162, <https://doi.org/10.1109/JSTARS.2013.2238892>, 2013.